8

THE FINITE-DIFFERENCE TIME-DOMAIN METHOD FOR NUMERICAL MODELING OF ELECTROMAGNETIC WAVE INTERACTIONS WITH ARBITRARY STRUCTURES

A. Taflove and K. R. Umashankar

8.1 Introduction

Accurate numerical modeling of full-vector electromagnetic wave interactions with arbitrary structures is difficult. Typical structures of engineering interest have shapes, apertures, cavities, and material compositions or surface loadings which produce near fields that cannot be resolved into finite sets of modes or rays. Proper numerical modeling of such near fields requires sampling at sub-wavelength resolution to avoid aliasing of magnitude and phase information. The goal is to provide a self-consistent model of the mutual coupling of the electrically-small cells comprising the structure.

This chapter reviews the formulation and applications of a candidate numerical modeling approach for this purpose: the finite-difference time-domain (FD-TD) solution of Maxwell's curl equations. FD-TD is very simple in concept and execution. However, it is remarkably robust, providing highly accurate modeling predictions for a wide variety of electromagnetic wave interaction problems. FD-TD is

analogous to existing finite-difference solutions of scalar wave propagation and fluid-flow problems in that the numerical model is based upon a direct, time-domain solution of the governing partial differential equation. Yet, FD-TD is a non-traditional approach to numerical electromagnetics for engineering applications where frequency-domain integral equation approaches have dominated for 25 years.

One of the goals of this chapter is to demonstrate that recent advances in FD-TD modeling concepts and software implementation, combined with advances in computer technology, have expanded the scope, accuracy, and speed of FD-TD modeling to the point where it may be the preferred choice for complex electromagnetic wave penetration, scattering, guiding, and inverse scattering problems. With this in mind, this chapter will succinctly review the following FD-TD modeling validations and examples:

1. Electromagnetic wave scattering, two dimensions
    a. Square metal cylinder, TM polarization
    b. Circular muscle-fat layered cylinder, TE polarization
    c. Homogeneous, anisotropic, square material cylinder
    d. Circular metal cylinder, conformally modeled
    e. Flanged metal open cavity
    f. Relativistically vibrating mirror, oblique incidence
2. Electromagnetic wave scattering, three dimensions
    a. Metal cube, broadside incidence
    b. Flat conducting plate, multiple monostatic looks
    c. T-shaped conducting target, multiple monostatic looks
3. Electromagnetic wave penetration and coupling in 2-D and 3-D
    a. Narrow slots and lapped joints in thick screens
    b. Wires and wire bundles in free space and in a metal cavity
4. Very complex three-dimensional structures
    a. Missile seeker section
    b. Inhomogeneous tissue model of the entire human body
5. Microstrip and microwave circuit models
6. Inverse scattering reconstructions in one and two dimensions

Finally, this chapter will conclude with a discussion of computing resources for FD-TD and the potential impact of massively concurrent machines.

8.2 General Characteristics of FD-TD

As stated, FD-TD is a direct solution of Maxwell's time-dependent curl equations. It employs no potential. Instead, it applies simple, second-order accurate central-difference approximations [1] for the space and time derivatives of the electric and magnetic fields directly to the respective differential operators of the curl equations. This achieves a sampled-data reduction of the continuous electromagnetic field in a volume of space, over a period of time. Space and time discretizations are selected to bound errors in the sampling process, and to insure numerical stability of the algorithm [2]. Electric and magnetic field components are interleaved in space to permit a natural satisfaction of tangential field continuity conditions at media interfaces. Overall, FD-TD is a marching-in-time procedure which simulates the continuous actual waves by sampled-data numerical analogs propagating in a data space stored in a computer. At each time step, the system of equations to update the field components is fully explicit, so that there is no need to set up or solve a set of linear equations, and the required computer storage and running time is proportional to the electrical size of the volume modeled.

Figure 1(a) illustrates the time-domain wave tracking concept of the FD-TD method. A region of space within the dashed lines is selected for field sampling in space and time. At time = 0, it is assumed that all fields within the numerical sampling region are identically zero. An incident plane wave is assumed to enter the sampling region at this point. Propagation of the incident wave is modeled by the commencement of time-stepping, which is simply the implementation of the finite-difference analog of the curl equations. Time-stepping continues as the numerical analog of the incident wave strikes the modeled target embedded within the sampling region. All outgoing scattered wave analogs ideally propagate through the lattice truncation planes with negligible reflection to exit the sampling region. Phenomena such as induction of surface currents, scattering and multiple scattering, penetration through apertures, and cavity excitation are modeled time-step by time-step by the action of the curl equations analog. Self-consistency of these modeled phenomena is generally assured if their spatial and temporal variations are well resolved by the space and time sampling process.

Time-stepping is continued until the desired late-time pulse response or steady-state behavior is observed. An important example of

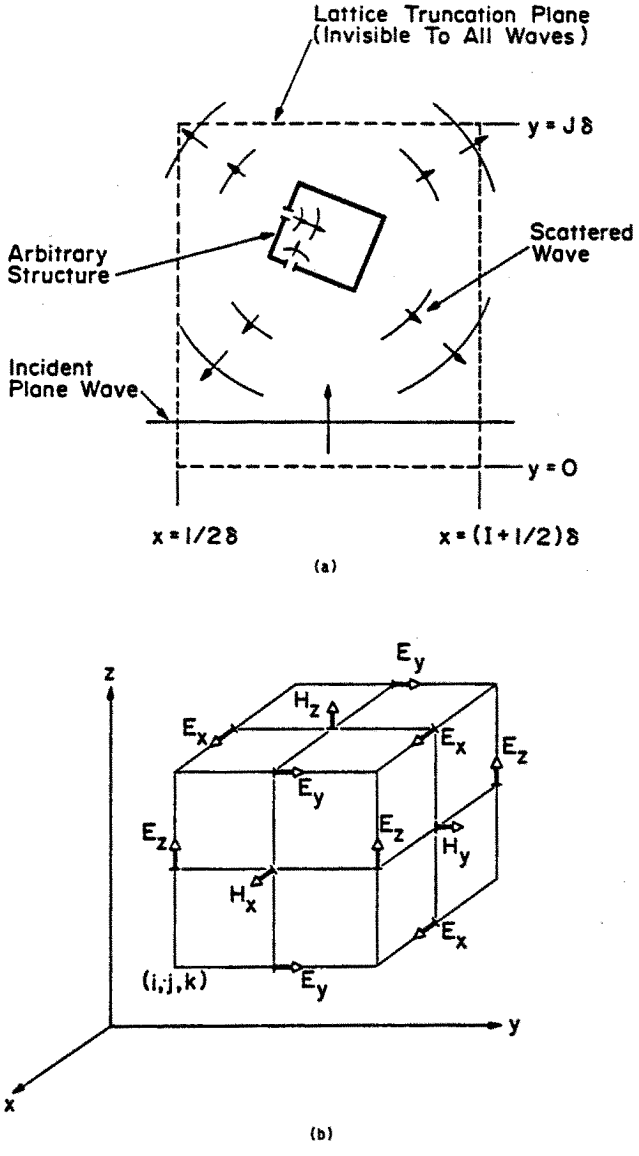

Figure 1 Basic elements of the FD-TD space lattice: (a) Time-domain wave tracking concept; (b) Lattice unit cell in Cartesian coordinates [1].

the latter is the sinusoidal steady state, wherein the incident wave is assumed to have a sinusoidal dependence, and time-stepping is continued until all fields in the sampling region exhibit sinusoidal repetition. This is a consequence of the limiting amplitude principle [3]. Extensive numerical experimentation with FD-TD has shown that the number of complete cycles of the incident wave required to be time-stepped to achieve the sinusoidal steady state is approximately equal to the Q factor of the structure or phenomenon being modeled.

Figure 1(b) illustrates the positions of the electric and magnetic field components about a unit cell of the FD-TD lattice in Cartesian coordinates [1]. Note that each magnetic field vector component is surrounded by four circulating electric field vector components, and vice versa. This arrangement permits not only a centered-difference analog to the space derivatives of the curl equations, but also a natural geometry for implementing the integral form of Faraday's law and Ampere's Law at the space-cell level. This integral interpretation permits a simple but effective modeling of the physics of thin-slot coupling, thin-wire coupling, and smoothly curved target surfaces, as will be seen later.

Figure 2 illustrates how an arbitrary three-dimensional scatterer is embedded in an FD-TD space lattice comprised of the unit cells of Fig. 1(b). Simply, the desired values of electrical permittivity and conductivity are assigned to each electric field component of the lattice. Correspondingly, desired values of magnetic permeability and equivalent conductivity are assigned to each magnetic field component of the lattice. The media parameters are interpreted by the FD-TD program as local coefficients for the time-stepping algorithm. Specification of media properties in this component-by-component manner results in a stepped-edge, or staircase approximation of curved surfaces. Continuity of tangential fields is assured at the interface of dissimilar media with this procedure. There is no need for special field matching at media interface points. Stepped-edge approximation of curved surfaces has been found to be adequate in the FD-TD modeling problems studied in the 1970's and early 1980's, including wave interactions with biological tissues [4], penetration into cavities [5,6], and electromagnetic pulse (EMP) interactions with complex structures [7–9]. However, recent interest in wide dynamic range models of scattering by curved targets has prompted the development of surface-conforming FD-TD approaches which eliminate staircasing. These will be summarized later in this chapter.

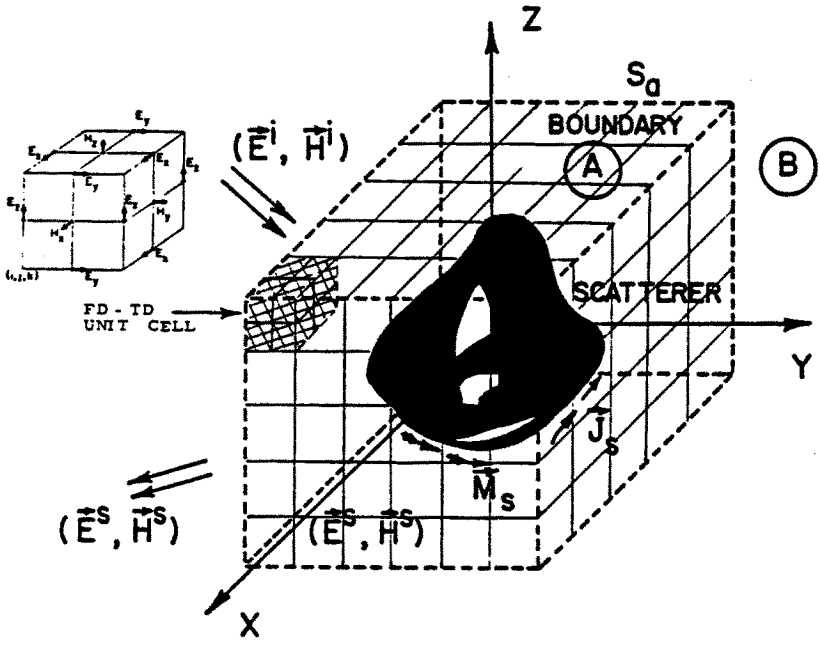

Figure 2 Arbitrary 3-D scatterer embedded in a FD-TD lattice.

8.3 Basic FD-TD Algorithm Details

a. *Maxwell's Curl Equations*

Consider a region of space which is source-free and has constitutive electrical parameters that are independent of time. Then, using the MKS system of units, Maxwell's curl equations are given by

$$\frac{\partial \overline{H}}{\partial t} = -\frac{1}{\mu}\nabla \times \overline{E} - \frac{\rho'}{\mu}\overline{H} \tag{1}$$

$$\frac{\partial \overline{E}}{\partial t} = \frac{1}{\epsilon}\nabla \times \overline{H} - \frac{\sigma}{\epsilon}\overline{E} \tag{2}$$

where $\overline{E}$ is the electric field in volts/meter; $\overline{H}$ is the magnetic field in amperes/meter; ϵ is the electrical permittivity in farads/meter; σ is the electrical conductivity in mhos/meter (siemens/meter); μ is the magnetic permeability in henrys/meter; and ρ' is an equivalent mag-

netic resistivity in ohms/meter. (The magnetic resistivity term is provided to yield symmetric curl equations, and allow for the possibility of a magnetic field loss mechanism.) Assuming that ϵ, σ, μ, and ρ' are isotropic, the following system of scalar equations is equivalent to Maxwell's curl equations in the rectangular coordinate system (x, y, z)

$$\frac{\partial H_x}{\partial t} = \frac{1}{\mu}\left(\frac{\partial E_y}{\partial z} - \frac{\partial E_z}{\partial y} - \rho' H_x\right) \tag{3a}$$

$$\frac{\partial H_y}{\partial t} = \frac{1}{\mu}\left(\frac{\partial E_z}{\partial x} - \frac{\partial E_x}{\partial z} - \rho' H_y\right) \tag{3b}$$

$$\frac{\partial H_z}{\partial t} = \frac{1}{\mu}\left(\frac{\partial E_x}{\partial y} - \frac{\partial E_y}{\partial x} - \rho' H_z\right) \tag{3c}$$

$$\frac{\partial E_x}{\partial t} = \frac{1}{\epsilon}\left(\frac{\partial H_z}{\partial y} - \frac{\partial H_y}{\partial z} - \sigma E_x\right) \tag{4a}$$

$$\frac{\partial E_y}{\partial t} = \frac{1}{\epsilon}\left(\frac{\partial H_x}{\partial z} - \frac{\partial H_z}{\partial x} - \sigma E_y\right) \tag{4b}$$

$$\frac{\partial E_z}{\partial t} = \frac{1}{\epsilon}\left(\frac{\partial H_y}{\partial x} - \frac{\partial H_x}{\partial y} - \sigma E_z\right) \tag{4c}$$

The system of six coupled partial differential equations of (3) and (4) forms the basis of the FD-TD algorithm for electromagnetic wave interactions with general three-dimensional objects. Before proceeding with the details of the algorithm, it is informative to consider one important simplification of the full three-dimensional case. Namely, if we assume that neither the incident plane wave excitation nor the modeled geometry has any variation in the z-direction (i.e., all partial derivatives with respect to z equal zero), Maxwell's curl equations reduce to two decoupled sets of scalar equations. These decoupled sets, termed the transverse magnetic (TM) mode and the transverse electric (TE) mode, describe two-dimensional wave interactions with objects. The relevant equations for each case follow

TM case (E_z, H_x, and H_y field components only)

$$\frac{\partial H_x}{\partial t} = -\frac{1}{\mu}\left(\frac{\partial E_z}{\partial y} + \rho' H_x\right) \tag{5a}$$

$$\frac{\partial H_y}{\partial t} = \frac{1}{\mu}\left(\frac{\partial E_z}{\partial x} - \rho' H_y\right) \tag{5b}$$

$$\frac{\partial E_z}{\partial t} = \frac{1}{\epsilon}\left(\frac{\partial H_y}{\partial x} - \frac{\partial H_x}{\partial y} - \sigma E_z\right) \tag{5c}$$

TE case (H_z, E_x, and E_y field components only)

$$\frac{\partial E_x}{\partial t} = \frac{1}{\epsilon}\left(\frac{\partial H_z}{\partial y} - \sigma E_x\right) \tag{6a}$$

$$\frac{\partial E_y}{\partial t} = -\frac{1}{\epsilon}\left(\frac{\partial H_z}{\partial x} + \sigma E_y\right) \tag{6b}$$

$$\frac{\partial H_z}{\partial t} = \frac{1}{\mu}\left(\frac{\partial E_x}{\partial y} - \frac{\partial E_y}{\partial x} - \rho' H_z\right) \tag{6c}$$

b. *The Yee Algorithm*

In 1966, Yee [1] introduced a set of finite-difference equations for the system of (3) and (4). Following Yee's notation, we denote a space point in a rectangular lattice as

$$(i, j, k) = (i\Delta x, j\Delta y, k\Delta z) \tag{7a}$$

and any function of space and time as

$$F^n(i, j, k) = F(i\Delta x, j\Delta y, k\Delta z, n\Delta t) \tag{7b}$$

where $\Delta x, \Delta y$, and Δz are, respectively, the lattice space increments in the x, y, and z coordinate directions; Δt is the time increment; and i, j, k, and n are integers. Yee used centered finite-difference expressions for the space and time derivatives that are both simply programmed and second-order accurate in the space and time increments, respectively:

$$\frac{\partial F^n(i, j, k)}{\partial x} = \frac{F^n(i + \frac{1}{2}, j, k) - F^n(i - \frac{1}{2}, j, k)}{\Delta x} + O(\Delta x^2) \tag{8a}$$

$$\frac{\partial F^n(i, j, k)}{\partial t} = \frac{F^{n+\frac{1}{2}}(i, j, k) - F^{n-\frac{1}{2}}(i, j, k)}{\Delta t} + O(\Delta t^2) \tag{8b}$$

To achieve the accuracy of (8a), and to realize all of the required space derivatives of the system of (3) and (4), Yee positioned the components of $\overline{E}$ and $\overline{H}$ about a unit cell of the lattice as shown in Fig. 1(b). To achieve the accuracy of (8b), he evaluated $\overline{E}$ and $\overline{H}$ at alternate half time steps. The following are sample finite-difference time-stepping expressions for a magnetic and an electric field component resulting from these assumptions

$$H_x^{n+\frac{1}{2}}(i,j+\tfrac{1}{2},k+\tfrac{1}{2}) =$$

$$\frac{1-\frac{\rho'(i,j+1/2,k+1/2)\Delta t}{2\mu(i,j+1/2,k+1/2)}}{1+\frac{\rho'(i,j+1/2,k+1/2)\Delta t}{2\mu(i,j+1/2,k+1/2)}} \cdot H_x^{n-\frac{1}{2}}(i,j+\tfrac{1}{2},k+\tfrac{1}{2})$$

$$+\frac{\Delta t}{\mu(i,j+\frac{1}{2},k+\frac{1}{2})} \cdot \frac{1}{1+\frac{\rho'(i,j+1/2,k+1/2)\Delta t}{2\mu(i,j+1/2,k+1/2)}} \cdot \tag{9}$$

$$\left\{ \begin{array}{l} [E_y^n(i,j+\frac{1}{2},k+1) - E_y^n(i,j+\frac{1}{2},k)]/\Delta z + \\ [E_z^n(i,j,k+\frac{1}{2}) - E_z^n(i,j+1,k+\frac{1}{2})]/\Delta y \end{array} \right\}$$

$$E_z^{n+1}(i,j,k+\tfrac{1}{2}) = \frac{1-\frac{\sigma(i,j,k+\frac{1}{2})\Delta t}{2\epsilon(i,j,k+1/2)}}{1+\frac{\sigma(i,j,k+1/2)\Delta t}{2\epsilon(i,j,k+1/2)}} \cdot E_z^n(i,j,k+\tfrac{1}{2})$$

$$+\frac{\Delta t}{\epsilon(i,j,k+\frac{1}{2})} \cdot \frac{1}{1+\frac{\sigma(i,j,k+1/2)\Delta t}{2\epsilon(i,j,k+1/2)}} \cdot \tag{10}$$

$$\left\{ \begin{array}{l} [H_y^{n+\frac{1}{2}}(i+\frac{1}{2},j,k+\frac{1}{2}) - H_y^{n+\frac{1}{2}}(i-\frac{1}{2},j,k+\frac{1}{2})]/\Delta x + \\ [H_x^{n+\frac{1}{2}}(i,j-\frac{1}{2},k+\frac{1}{2}) - H_x^{n+\frac{1}{2}}(i,j+\frac{1}{2},k+\frac{1}{2})]/\Delta y \end{array} \right\}$$

With the system of finite-difference equations represented by (9) and (10), the new value of a field vector component at any lattice point depends only on its previous value and on the previous values of the

components of the other field vector at adjacent points. Therefore, at any given time step, the computation of a field vector can proceed either one point at a time; or, if p parallel processors are employed concurrently, p points at a time.

c. *Numerical Stability*

To insure the stability of the time-stepping algorithm exemplified by (9) and (10), Δt is chosen to satisfy the inequality [2,10]

$$\Delta t \leq \frac{1}{c_{\max}\left\{\frac{1}{\Delta x^2}+\frac{1}{\Delta y^2}+\frac{1}{\Delta z^2}\right\}^{\frac{1}{2}}} \tag{11}$$

where c_{max} is the maximum electromagnetic wave phase velocity within the media being modeled. Note that the corresponding numerical stability criterion set forth in Eqs. (7) and (8) of Reference [1] is incorrect [2]. For the TM and TE two-dimensional modeling cases, it can be shown [10] that the modified time-step limit for numerical stability is obtained from (11) simply by setting $\Delta z = \infty$.

d. *Numerical Dispersion*

The numerical algorithm for Maxwell's curl equations represented by (9) and (10) causes dispersion of the simulated wave modes in the computational lattice. That is, the phase velocity of numerical modes in the FD-TD lattice can vary with modal wavelength, direction of propagation, and lattice discretization. This numerical dispersion can lead to non-physical results such as pulse distortion, artificial anisotropy, and pseudo-refraction. Numerical dispersion is a factor in FD-TD modeling that must be accounted to understand the operation of the algorithm and its accuracy limits.

Following the analysis in [10], it can be shown that the numerical dispersion relation for the three-dimensional case represented by (9) and (10) is given by

$$\left(\frac{1}{c\Delta t}\right)^2 \sin^2\left(\frac{\omega\Delta t}{2}\right) = \frac{1}{\Delta x^2}\sin^2\left(\frac{k_x\Delta x}{2}\right) + \frac{1}{\Delta y^2}\sin^2\left(\frac{k_y\Delta y}{2}\right) + \frac{1}{\Delta z^2}\sin^2\left(\frac{k_z\Delta z}{2}\right) \tag{12}$$

where k_x, k_y, and k_z are, respectively, the x, y, and z components of the wavevector; ω is the wave angular frequency; and c is the speed of light in the homogeneous material being modeled.

In contrast to the numerical dispersion relation, the analytical dispersion relation for a plane wave in a continuous, lossless medium is just

$$\omega^2/c^2 = k_x^2 + k_y^2 + k_z^2 \tag{13}$$

for the three-dimensional case. Although, at first glance, (12) bears little resemblance to the ideal case of (13), we can easily show that (12) reduces to (13) in the limit as $\Delta t, \Delta x, \Delta y$, and Δx all go to zero. Qualitatively, this suggests that numerical dispersion can be reduced to any degree that is desired if we only use a fine-enough FD-TD gridding.

To quantitatively illustrate the dependence of numerical dispersion upon FD-TD grid discretization, we shall take as an example the two-dimensional TM case ($\Delta z = \infty$), assuming for simplicity square unit cells ($\Delta x = \Delta y = \delta$) and wave propagation at an angle α with respect to the positive x-axis ($k_x = k \cos \alpha$; $k_y = \sin \alpha$). Then, dispersion relation (12) simplifies to

$$\left(\frac{\delta}{c\Delta t}\right)^2 \sin^2\left(\frac{\omega \Delta t}{2}\right) = \sin^2\left(\frac{k\delta \cos\alpha}{2}\right) + \sin^2\left(\frac{k\delta \sin\alpha}{2}\right) \tag{14}$$

(14) can be conveniently solved for the wavevector magnitude, k, by applying Newton's method. This process is especially convenient if δ is normalized to the free-space wavelength.

Figure 3a provides results using this procedure which illustrate the variation of numerical phase velocity with wave propagation angle in the FD-TD grid [10]. Three different grid resolutions of the propagating wave are examined: coarse ($\lambda_0/5$); normal ($\lambda_0/10$); and fine ($\lambda_0/20$). For each resolution, the relation $c\Delta t = \delta/2$ was maintained. This relation is commonly used in two- and three-dimensional FD-TD codes to satisfy the numerical stability criterion of (11) with ample safety margin. From Fig. 3a, it is seen that the numerical phase velocity is maximum at 45° (oblique incidence), and minimum at 0° and 90° (incidence along either Cartesian grid axis) for all grid resolutions. This represents a numerical anisotropy that is inherent in the Yee algorithm. However, the velocity error relative to the ideal case diminishes by approximately a 4:1 factor each time that the grid cell size is halved,

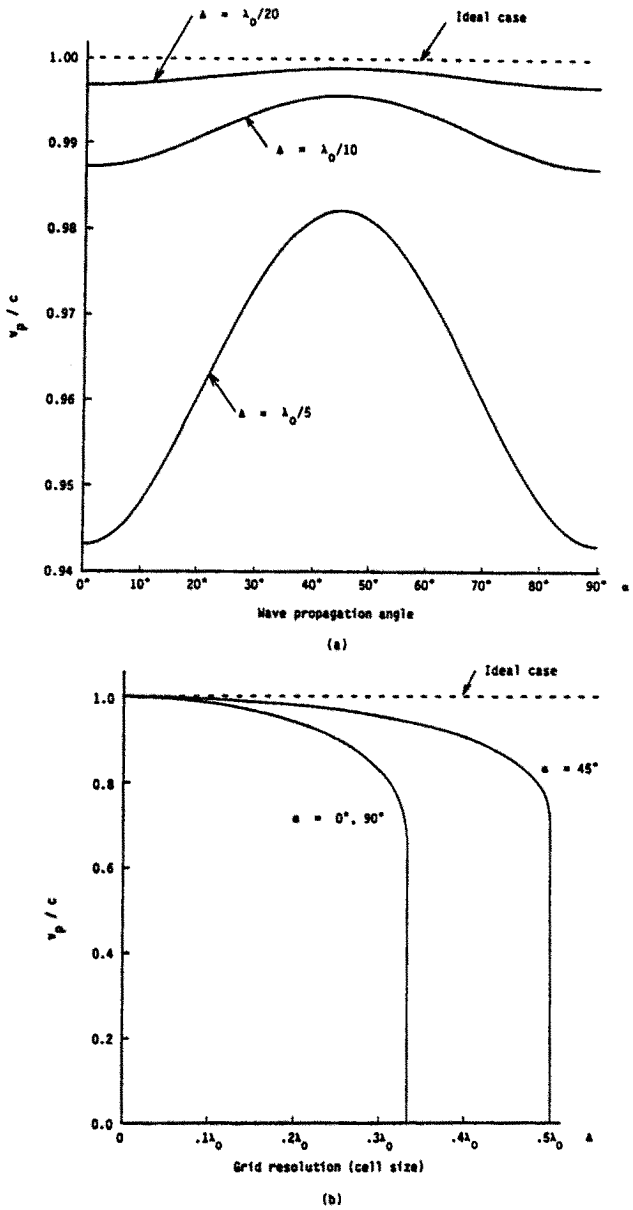

Figure 3 Variation of FD-TD numerical wave phase velocity (dispersion): (a) with wave propagation angle in the grid for three different grid discretizations; (b) with grid resolution for three different wave propagation angles [10].

so that the worst-case velocity error for the normal resolution case is only -1.3%, and only -0.31% for the fine resolution case.

Figure 3(b) graphs the variation of numerical phase velocity with grid resolution at the fixed incidence angles, 45° and 0°(90°). Again, the relation $c\Delta t = \delta/2$ was maintained for each resolution. Here, it is seen that the numerical phase velocity at each angle of incidence diminishes as the propagating wave is more coarsely resolved, eventually reaching a sharp threshold where the numerical phase velocity goes to zero and the wave can no longer propagate in the FD-TD grid. This represents a numerical low-pass filtering effect that is inherent in the Yee algorithm, wherein the wavelength of propagating numerical modes has a lower bound of 2 to 3 space cells, depending upon the propagation direction. As a result, FD-TD modeling of pulses having finite duration (and thus, infinite bandwidth) can result in progressive pulse distortion as higher spatial frequency components propagate more slowly than lower spatial frequency components, and very high spatial frequency components with wavelengths less than 2 to 3 cells are rejected. This numerical dispersion causes broadening of finite-duration pulses, and leaves a residue of high-frequency ringing on the trailing edges due to the relatively slowly propagating high-frequency components. From Figs. 3(a) and 3(b), we see that pulse distortion can be bounded by obtaining the Fourier spatial frequency spectrum of the desired pulse, and selecting a grid cell size so that the principal spectral components are resolved with at least 10 cells per wavelength. This would limit the spread of numerical phase velocities of the principal spectral components to less than 1%, regardless of wave propagation angle in the grid.

In addition to numerical phase velocity anisotropy and pulse distortion effects, numerical dispersion can lead to pseudo-refraction of propagating modes if the grid cell size is a function of position in the grid. Such variable-cell gridding would also vary the grid resolution of propagating numerical modes, and thereby perturb the modal phase velocity distribution. This would lead to non-physical reflection and refraction of numerical modes at interfaces of grid regions having different cell sizes (even if these interfaces were located in free space), just as physical waves undergo reflection and refraction at interfaces of dielectric media having different indices of refraction. The degree of non-physical refraction is dependent upon the magnitude and abruptness of the change of the modal phase velocity distribution, and can be estimated by using conventional theory for wave refraction at dielectric

interfaces.

We have stated that, in the limit of infinitesimal Δt and δ, (12) reduces to (13), the ideal dispersion case. This reduction also occurs if Δt, δ, and the direction of propagation are suitably chosen. For example, in a three-dimensional cubic lattice, reduction to the ideal dispersion case can be demonstrated for wave propagation along a lattice diagonal ($k_x = k_y = k_z = k/\sqrt{3}$) and $\Delta t = \delta/(c\sqrt{3})$ (exactly the limit set by numerical stability). Similarly, in a two-dimensional square grid, the ideal dispersion case can be demonstrated for wave propagation along a grid diagonal ($k_x = k_y = k/\sqrt{2}$) and $\Delta t = \delta/(c\sqrt{2})$ (again the limit set by numerical stability). Finally, in one dimension, the ideal case is obtained for $\Delta t = \delta/c$ (again the limit set by numerical stability) for all propagating modes.

e. Lattice Zoning and Plane Wave Source Condition

The numerical algorithm for Maxwell's curl equations defined by the finite-difference system reviewed above has a linear dependence upon the components of the electromagnetic field vectors. Therefore, this system can be applied with equal validity to either the incident-field vector components, the scattered-field vector components, or the total-field vector components (the sum of incident plus scattered). Present FD-TD codes utilize this property to zone the numerical space lattice into two distinct regions, as shown in Fig. 4(a), separated by a rectangular virtual surface which serves to connect the fields in each region [11,12].

Region 1, the inner region of the FD-TD lattice, is denoted as the total- field region. Here, it is assumed that the finite-difference system for the curl equations operates on total-field vector components. The interacting structure of interest is embedded within this region.

Region 2, the outer region of the FD-TD lattice, is denoted as the scattered-field region. Here, it is assumed that the finite-difference system for the curl equations operates only on scattered-field vector components. This implies that there is no incident wave in Region 2. The outer lattice planes bounding Region 2, called the lattice truncation planes, serve to implement the free-space radiation condition (discussed in the next section) which simulates the field sampling space extending to infinity.

The total-field/scattered-field lattice zoning illustrated in Fig. 4(a) provides a number of key features which enhance the computational

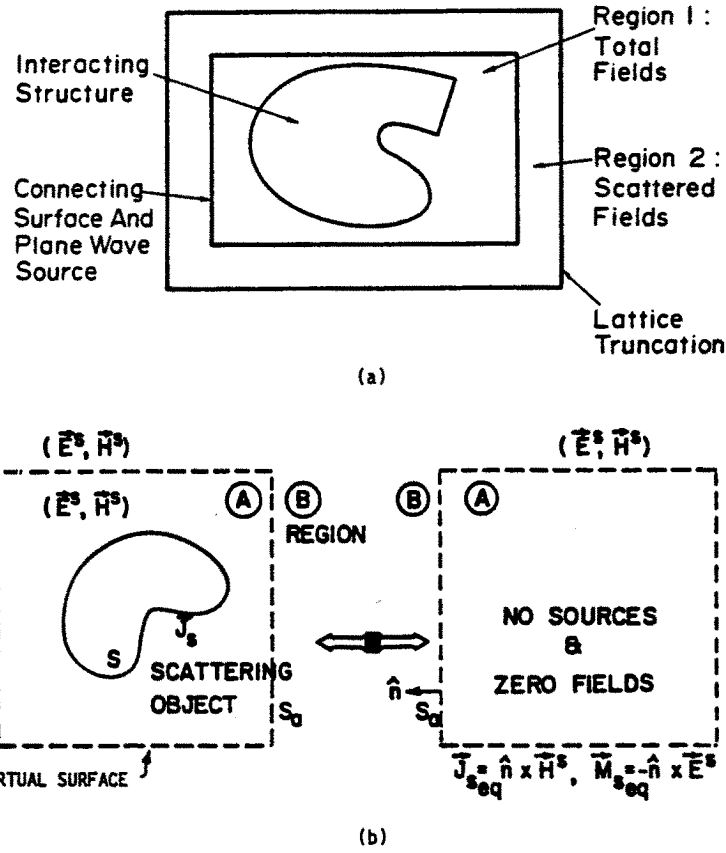

Figure 4 Zoning of the FD-TD lattice: (a) Total field and scattered field regions [11,12]; (b) Near-to-far field integration surface located in the scattered field region [12].

flexibility and dynamic range of the FD-TD method:

Arbitrary incident wave. The connecting condition provided at the interface of the inner and outer regions, which assures consistency of the numerical space derivative operations across the interface, simultaneously generates an arbitrary incident plane wave in Region 1 having a user-specified time waveform, angle of incidence, and angle of polarization. This connecting condition, discussed in detail in [10], almost completely confines the incident wave to Region 1 and yet is transparent to outgoing scattered wave modes which are free to enter Region 2.

Simple programming of inhomogeneous structures. The required continuity of total tangential E and H fields across the interface of dissimilar media is automatically provided by the original Yee algorithm if the media are located in a zone (such as Region 1) where total fields are time-marched. This avoids the problems inherent in a pure scattered-field code where enforcement of the continuity of total tangential fields is a separate process requiring the incident field to be computed at all interfaces of dissimilar media, and then added to the values of the time-marched scattered fields at the interfaces. Clearly, computation of the incident field at numerous points along possibly complex, structure-specific loci is likely to be much more involved than computation of the incident field only along the simple connecting surface between Regions 1 and 2 (needed to implement the total-field/scattered-field zoning). The latter surface has a fixed locus that is independent of the shape or complexity of the interaction structure that is embedded in Region 1.

Wide computational dynamic range. Low levels of the total field in deep shadow regions or cavities of the interaction structure are computed directly by time-marching total fields in Region 1. In a pure scattered-field code, however, the low levels of total field are obtained by computing the incident field at each desired point, and then adding to the values of the time-marched scattered fields. Thus, it is seen that a pure scattered-field code relies upon near cancellation of the incident and scattered field components of the total field to obtain accurate results in deep shadow regions and cavities. An undesirable hallmark of this cancellation is contamination of the resultant low total-field levels by subtraction noise, wherein slight percentage errors in calculating the scattered fields result in possibly very large percentage errors in the residual total fields. By time-marching total fields directly, the zoned FD-TD code avoids subtraction noise in Region 1 and achieves a computational dynamic range more than 30 dB greater than that for a pure scattered-field code.

Far-field response. The provision of a well-defined scattered-field region in the FD-TD lattice permits the near-to-far field transformation illustrated in Fig. 4(b) [12]. The dashed virtual surface shown in Fig. 4(b) can be located along convenient lattice planes in the scattered-field region of Fig. 4(a). Tangential scattered E and H fields computed via FD-TD at this virtual surface can then be weighted by the free-space Green's function and then integrated (summed) to provide the

far-field response and radar cross section (full bistatic response for the assumed illumination angle) [12–14]. The near-field integration surface has a fixed rectangular shape, and thus is independent of the shape or composition of the enclosed structure being modeled.

8.4 Contour Path Interpretation

a. Usefulness

The Yee algorithm for FD-TD was originally interpreted as a direct approximation of the pointwise derivatives of Maxwell's time-dependent curl equations by using numerical central differences [1]. Although this interpretation is useful for understanding how FD-TD models wave propagation away from material surfaces, it sheds little light on what algorithm modifications are needed to properly model the physics of fine geometrical features such as wires, slots, and curved surfaces requiring sub-cell spatial resolution. Modeling of such features has become increasingly important as confidence in the basic predictive powers of FD-TD has grown.

Recent work has indicated that extension of FD-TD modeling to wires, slots, and curved surfaces can be achieved by departing from Yee's original pointwise derivative interpretation. As shown in Fig. 5, the new idea involves starting with a more macroscopic (but still local) combined-field description based upon Ampere's Law and Faraday's Law in *integral* form, implemented on an array of electrically small, spatially orthogonal contours. These contours mesh (intersect) in the manner of links in a chain, providing a geometrical interpretation of the coupling of Ampere's Law and Faraday's Law. This meshing results in the filling of the FD-TD modeled space by a three-dimensional chain-link array of intersecting, orthogonal contours. The presence of wires, slots, and curved surfaces can be accounted by incorporating appropriate field behavior into the contour and surface integrals implementing Ampere's Law and Faraday's Law at selected meshes, and by deforming contour paths as required to conform with surface curvature.

b. Equivalence to the Yee Algorithm in Free Space

We shall first demonstrate the equivalence of the Yee and contour path interpretations for the free-space case [15]. For simplicity, FD-TD expressions will be developed for only one field component in Fig. 5(a)

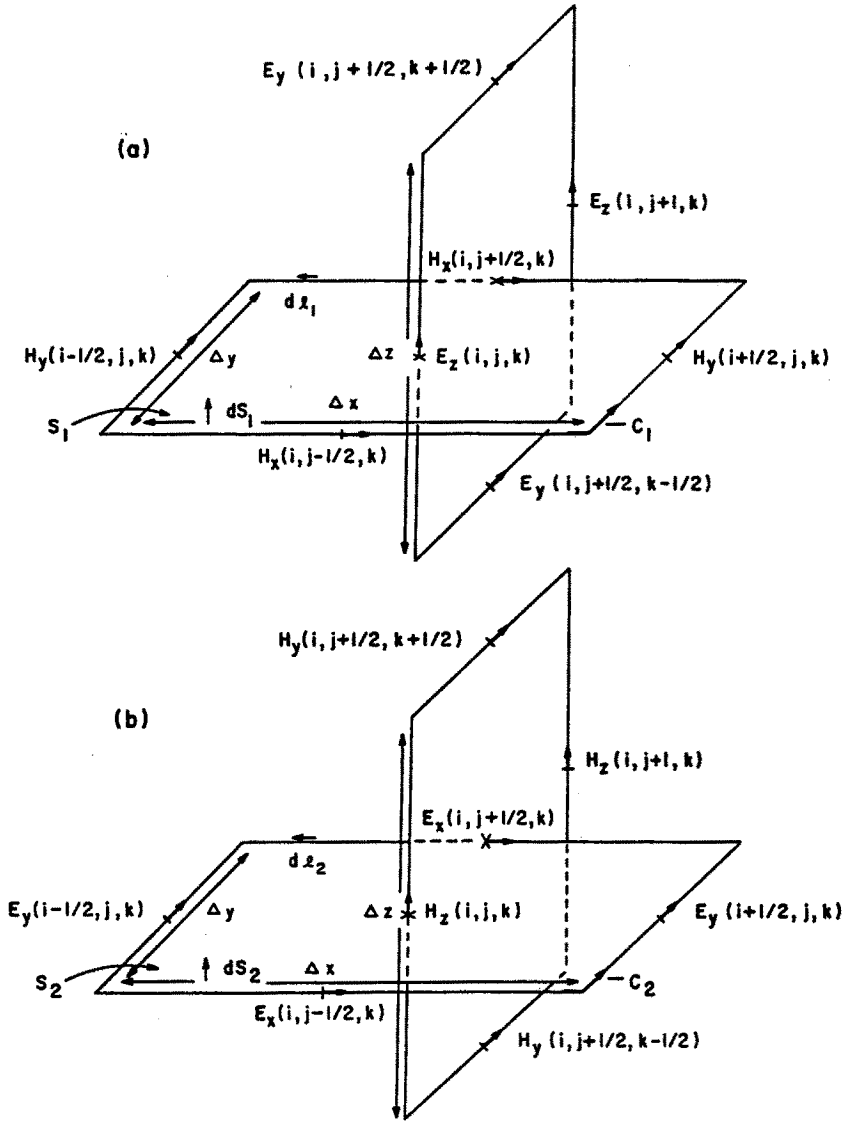

Figure 5 Examples of spatially orthogonal contours in free space: (a) Ampere's Law for E_x; (b) Faraday's Law for H_x [15].

and one field component in Fig. 5(b); extension to all of the rest will be seen to be straightforward.

Applying Ampere's Law along C_1 in Fig. 5(a), and assuming that the field value at a midpoint of one side of the contour equals the average value of that field component along that side, we obtain

$$\frac{\partial}{\partial t}\int_{S_1} \overline{D}\cdot d\overline{S}_1 = \oint_{C_1} \overline{H}\cdot \overline{dl}_1 \tag{15a}$$

$$\frac{\partial}{\partial t}\int_{S_1} \epsilon_0 E_z(i,j,k)dS_1 \simeq H_x(i,j-\tfrac{1}{2},k)\Delta x + H_y(i+\tfrac{1}{2},j,k)\Delta y - H_x(i,j+\tfrac{1}{2},k)\Delta x - H_y(i-\tfrac{1}{2},j,k)\Delta y \tag{15b}$$

Now, further assuming that $E_z(i,j,k)$ equals the average value of E_z over the surface, S_1; that $\Delta x = \Delta y = \delta$; and that the time derivative can be numerically realized by using a central-difference expression, (15b) reduces to

$$\epsilon_0\delta^2\cdot\left[\frac{E_z^{n+1}(i,j,k)-E_z^n(i,j,k)}{\Delta t}\right] = \left[\begin{array}{l} H_x^{n+\frac{1}{2}}(i,j-\frac{1}{2},k) - H_x^{n+\frac{1}{2}}(i,j+\frac{1}{2},k) + \\ H_y^{n+\frac{1}{2}}(i+\frac{1}{2},j,k) - H_y^{n+\frac{1}{2}}(i-\frac{1}{2},j,k) \end{array}\right]\cdot\delta \tag{15c}$$

where the superscripts indicate field values at time steps $n, n+\frac{1}{2}$, and $n+1$. Isolation of $E_z^{n+1}(i,j,k)$ on the left hand side then yields exactly the Yee time-stepping expression for E_z for the free-space case that was obtained directly from implementing the curl $\overline{H}$ equation.

In an analogous manner, we can apply Faraday's Law along contour C_2 in Fig. 5(b) to obtain:

$$\frac{\partial}{\partial t}\int_{S_2} \overline{B}\cdot d\overline{S}_2 = -\oint_{C_2} \overline{E}\cdot \overline{dl}_2 \tag{16a}$$

$$\frac{\partial}{\partial t}\int_{S_2} \mu_0 H_z(i,j,k)dS_2 \simeq -E_x(i,j-\tfrac{1}{2},k)\Delta x - E_y(i+\tfrac{1}{2},j,k)\Delta y + E_x(i,j+\tfrac{1}{2},k)\Delta x + E_y(i-\tfrac{1}{2},j,k)\Delta y \tag{16b}$$

$$\mu_0 \delta^2 \cdot \left[\frac{H_z^{n+\frac{1}{2}}(i,j,k) - H_z^{n-\frac{1}{2}}(i,j,k)}{\Delta t} \right] =$$

$$\left[\begin{array}{l} E_x^n(i, j+\frac{1}{2}, k) - E_x^n(i, j-\frac{1}{2}, k) + \\ \\ E_y(i-\frac{1}{2}, j, k) - E_y(i+\frac{1}{2}, j, k) \end{array} \right] \cdot \delta \qquad (16c)$$

Isolation of $H_z^{n+\frac{1}{2}}(i,j,k)$ on the left hand side yields exactly the Yee time-stepping expression for H_z, for the free-space case, that was obtained directly from implementing the curl $\overline{E}$ equation with finite differences.

c. *Example 1: Application to the Thin Slot*

To illustrate how the contour path interpretation provides the basis for FD-TD modeling of fine geometrical features requiring sub-cell spatial resolution, we first consider the thin slot in a planar, perfectly-conducting screen of finite size and thickness subjected to TE illumination [15]. Figure 6 illustrates the canonical slot geometry studied here, and the Faraday's Law contour paths, C_1, C_2, and C_3, used to derive special FD-TD algorithms for the longitudinal magnetic field components, H_z, located immediately adjacent to the screen.

The following briefly summarizes the assumptions concerning the near-field physics that are incorporated into the Faraday's Law models of Fig. 6. First, for contour C_1 (away from the slot), field components, H_z and E_y, are assumed to have no variation in the y direction (perpendicular to the screen). Evaluated at the x midpoint of contour C_1, H_z, and E_x are assumed to represent the average values of their respective fields over the full x interval. At contour C_2 (at the opening of the slot), H_z is assumed to represent the average value of the magnetic field over the entirety of the free-space part of S_2. Here, E_y is again assumed to have no variation in the y direction, and E_x is again assumed to represent the average value over the full x interval. At contour C_3 (within the slot), H_z is assumed to represent the average value of the magnetic field over the full y interval, and H_z and E_x are assumed to have no variation in the x direction (across the slot gap). Finally, for C_1, C_2, and C_3, the portions of the contours located within the conducting screen are assumed to have zero electric and magnetic

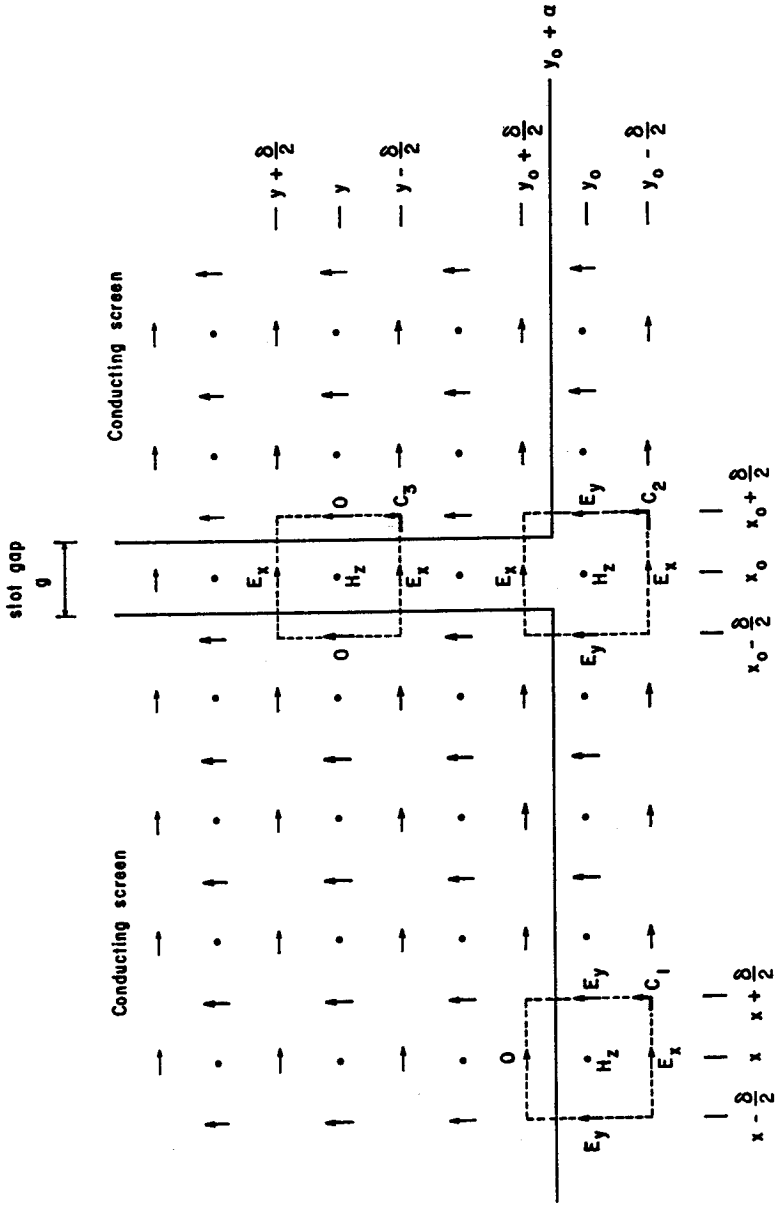

Figure 6 Faraday's Law contour paths for a 2-D planar conducting screen with a thin slot (TE case) [15].

fields.

After applying Faraday's Law of (16a) for the three contours subject to the above assumptions, the following special FD-TD time-stepping relations are obtained for the H_z components immediately adjacent to the screen

Away from the slot (contour C_1)

$$\frac{H_z^{n+\frac{1}{2}}(x,y_0) - H_z^{n-\frac{1}{2}}(x,y_0)}{\Delta t} \simeq$$

$$\frac{[E_y^n(x-\frac{\delta}{2},y_0) - E_y^n(x+\frac{\delta}{2},y_0)]\cdot(\frac{\delta}{2}+\alpha) - E_x^n(x,y_0-\frac{\delta}{2})\cdot\delta}{\mu_0\delta(\frac{\delta}{2}+\alpha)} \tag{17a}$$

At the opening (aperture) of the slot (contour C_2)

$$\frac{H_z^{n+\frac{1}{2}}(x_0,y_0) - H_z^{n-\frac{1}{2}}(x_0,y_0)}{\Delta t} \simeq$$

$$\frac{\begin{pmatrix} E_x^n(x_0,y_0+\frac{\delta}{2})\cdot g - E_x^n(x_0,y_0-\frac{\delta}{2})\cdot\delta + \\ [E_y^n(x_0-\frac{\delta}{2},y_0) - E_y^n(x_0+\frac{\delta}{2},y_0)]\cdot(\frac{\delta}{2}+\alpha) \end{pmatrix}}{\mu_0\cdot[\delta(\frac{\delta}{2}+\alpha)+g(\frac{\delta}{2}-\alpha)]} \tag{17b}$$

Within the slot (contour C_3)

$$\frac{H_z^{n+\frac{1}{2}}(x_0,y) - H_z^{n-\frac{1}{2}}(x_0,y)}{\Delta t} \simeq \frac{E_x^n(x_0,y+\frac{\delta}{2})\cdot g - E_x^n(x_0,y-\frac{\delta}{2})\cdot g}{\mu_0 g\delta} \tag{17c}$$

In (17c), we note that the slot gap distance, g, cancels on the right hand side, reducing the time-stepping relation for H_z in the slot to that of

a one-dimensional wave ($\pm y$-directed) in free space. For completeness, we also note that no magnetic or electric field components in the FD-TD space grid, other than the H_z components immediately adjacent to the screen, require modified time-stepping relations.

The accuracy of this contour integral model implemented on a coarse FD-TD grid (having 1/10 wavelength cell size) will be examined in section 8.8a for two cases: (1) a straight slot in a thick conducting screen; and (2) a U-shaped lapped joint in a thick conducting screen, exhibiting resonant transmission and gap-field phenomena. Excellent correspondence with high-resolution method of moments and FD-TD numerical benchmarks will be shown.

d. Example 2: Application to the Thin Wire

A second illustration of how the contour path interpretation permits incorporation of near-field physics (yielding special-purpose time-stepping expressions that were *not* obvious from the previous pure finite-difference perspective) is provided by considering coupling to a sub-cell diameter wire [16]. Figure 7 illustrates the Faraday's Law contour path used to derive the special FD-TD algorithm for the circumferential magnetic fields immediately adjacent to the wire. Although only H_y is shown, the analysis is easily generalized for the other adjacent, looping magnetic field components.

The following briefly summarizes the assumptions concerning the near-field physics that are incorporated into the Faraday's Law model. First, the near scattered circumferential magnetic field components and the near scattered radial electric field components are assumed to vary as $1/r$ near the wire, where r is the distance from the wire center. With r constrained to be less than 0.1 wavelength at any point in C (by FD-TD spatial resolution requirements), the $1/r$ singularity behavior of the scattered H_y and E_x fields is assumed to dominate the respective incident fields, so that the total H_y and E_x fields also take on the $1/r$ singularity. Finally, the near total H_y and the near total E_z fields, evaluated at the z midpoint of the contour, are assumed to represent the average values of their respective fields over the full z interval. These assumptions can be concisely summarized by the following expressions, assumed to apply on and within contour C of Fig. 7

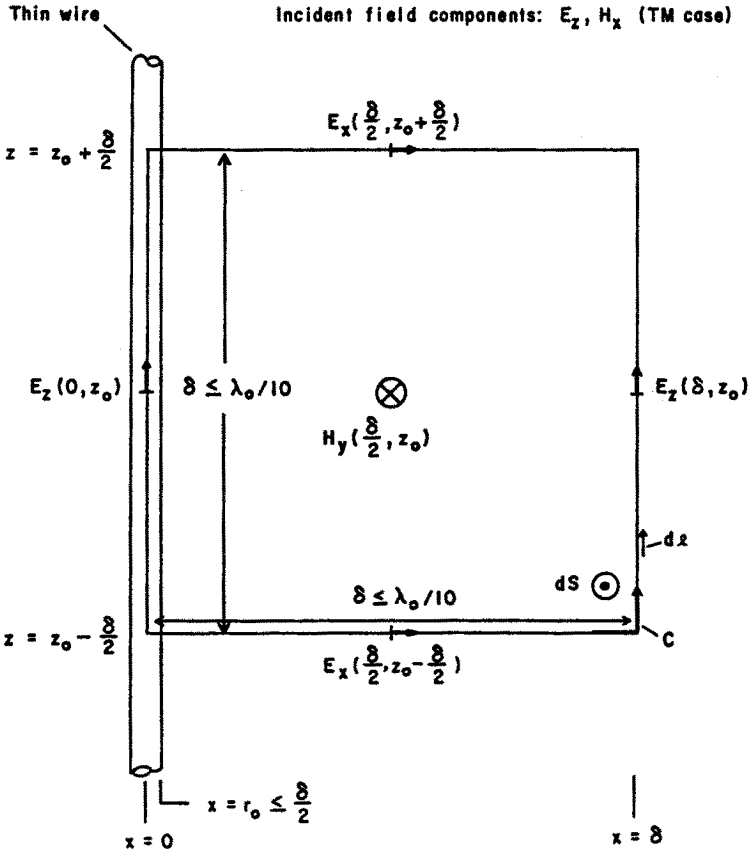

Figure 7 Faraday's Law contour path for thin-wire model [16].

$$H_y(x,z) \simeq H_y(\frac{\delta}{2}, z_0) \cdot \frac{(\frac{\delta}{2})}{x} \cdot [1 + c_1 \cdot (z - z_0)] \tag{18a}$$

$$E_x(x, z_0 \pm \frac{\delta}{2}) \simeq E_x(\frac{\delta}{2}, z_0 \pm \frac{\delta}{2}) \cdot \frac{(\frac{\delta}{2})}{x} \tag{18b}$$

$$E_z(0,z) = 0 \tag{18c}$$

$$E_z(\delta,z) \simeq E_z(\delta, z_0) \cdot [1 + c_2 \cdot (z - z_0)] \tag{18d}$$

where c_1 and c_2 are arbitrary constants that need not be known.

Using the field expressions of (18a)–(18d), we can now apply Faraday's Law of (16a) along contour C. We find that the $1/x$ variations in H_y and E_x yield natural logarithms. Further, the linear, odd symmetry variation in z assumed for H_y and E_z integrates out. This yields the following expression

$$\frac{H_y^{n+\frac{1}{2}}(\frac{\delta}{2}, z_0) - H_y^{n-\frac{1}{2}}(\frac{\delta}{2}, z_0)}{\Delta t} \simeq$$

$$\frac{[E_x^n(\frac{\delta}{2}, z_0 - \frac{\delta}{2}) - E_x^n(\frac{\delta}{2}, z_0 + \frac{\delta}{2})] \cdot \frac{1}{2} \ln\left(\frac{\delta}{r_0}\right) + E_z^n(\delta, z_0)}{\mu_0 \frac{\delta}{2} \ln\left(\frac{\delta}{r_0}\right)} \tag{19}$$

where r_0 (assumed to be less than 0.5 δ) is the wire radius. Isolation of $H_y^{n+\frac{1}{2}}(\frac{\delta}{2}, z_0)$ on the left hand side of (19) yields the required modified time-stepping relation. As stated, the analysis is easily generalized to obtain similar time-stepping relations for the other circumferential magnetic field components immediately adjacent to the wire. It should be noted that *no* other magnetic or electric field components in the FD-TD space lattice require modified time-stepping relations. All other field components are time-stepped by using the ordinary free-space Yee algorithm of section 8.3.

The accuracy of this contour integral model implemented on a coarse FD-TD grid will be examined in section 8.8b for four cases: (1) TM illumination of an infinitely long wire over a very wide range of wire radius; (2) broadside illumination of a two-wavelength long (antiresonant) dipole; (3) broadside illumination of a four-wire bundle where the entire bundle diameter is less than one space cell; and (4) coupling to a single wire and a wire-pair within an aperture-perforated metal cavity exhibiting a moderate-Q (30 to 80) resonant response. Excellent correspondence with either method of moments numerical results or experimental data will be shown.

8.5 Radiation Boundary Conditions

A basic consideration with the FD-TD approach to solve electromagnetic field problems is that most such problems are usually considered to be "open" problems where the domain of the computed field is ideally unbounded. Clearly, no computer can store an unlimited

amount of data, and therefore, the field computation zone must be limited in size. The computation zone must be large enough to enclose the structure of interest, and a suitable boundary condition on the outer perimeter of the computation zone must be used to simulate the extension of the computation zone to infinity. This boundary condition suppresses spurious reflections of outward-propagating wave analogs to some acceptable level, permitting the FD-TD solution to remain valid for all time steps (especially after spurious reflected wave analogs return to the vicinity of the modeled structure). Outer lattice boundary conditions of this type have been called either radiation boundary conditions (RBC's), absorbing boundary conditions (ABC's), or lattice truncation conditions.

The radiation condition cannot be directly obtained from the numerical algorithms for Maxwell's curl equations defined by the finite-difference systems reviewed in section 8.3. Principally, this is because these systems employ a central-difference scheme which requires knowledge of the field one-half space cell to each side of an observation point. Central differences cannot be implemented at the outermost lattice plane since, by definition, there is no information concerning the fields at points one-half space cell outside of the outermost lattice plane.

This section will develop the theory and numerical implementation of a very useful radiation condition in Cartesian coordinates. The radiation condition is appropriate for effectively truncating a two- or three-dimensional FD-TD space lattice with an overall level of spurious reflections of 1%–5% for outer lattice planes located 10-20 space cells from a target surface. The radiation condition will be derived using a recent theoretical approach, wave equation factoring. An approach to improvement of the currently used radiation boundary condition will also be summarized.

a. *One-Way Wave Equations*

A partial differential equation which permits wave propagation only in certain directions is called a "one-way wave equation." Figure 8 shows a finite, two-dimensional Cartesian domain, Ω, on which the time-dependent wave equation is to be simulated. In the interior of Ω, a numerical scheme (such as the algorithms of section 8.3) which models wave propagation in all directions is applied. On $\partial\Omega$, the outer boundary of Ω, only numerical wave motion that is outward from Ω is permitted. The boundary must permit outward propagating numerical

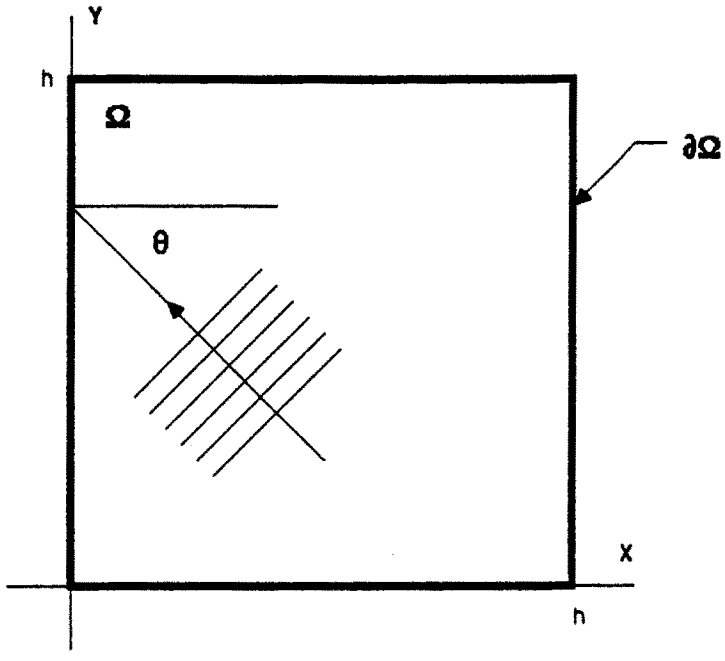

Figure 8 Numerical plane-wave analog incident upon left grid boundary of a 2-D Cartesian computational domain.

wave analogs to exit Ω just as if the simulation were performed on a computational domain of infinite extent. A scheme which enacts a one-way wave equation on $\partial\Omega$ for this purpose is called a radiation boundary condition (RBC).

b. Derivation by Wave Equation Factoring

The derivation of an RBC whose purpose is to absorb numerical waves incident upon the outer boundary of a finite-difference grid can be explained in terms of operator factoring. For example, consider the two-dimensional wave equation in Cartesian coordinates

$$U_{xx} + U_{yy} - \frac{1}{c^2} U_{tt} = 0 \tag{20}$$

where U is a scalar field component; the subscripts xx, yy, and tt denote second partial derivatives with respect to x, y, and t, respectively; and

c is the wave phase velocity. The partial differential operator here is

$$L \equiv D_x^2 + D_y^2 - \frac{1}{c^2} D_t^2 \tag{21a}$$

which uses the notation

$$D_x^2 \equiv \frac{\partial^2}{\partial x^2};\ D_y^2 \equiv \frac{\partial^2}{\partial y^2};\ D_t^2 \equiv \frac{\partial^2}{\partial t^2} \tag{21b}$$

The wave equation is then compactly written as

$$LU = 0 \tag{22}$$

The wave operator, L, can be factored in the following manner:

$$LU = L^+ L^- U = 0 \tag{23a}$$

where L^- is defined as

$$L^- \equiv D_x - \frac{D_t}{c}\sqrt{1 - S^2} \tag{23b}$$

with

$$S = \frac{D_y}{(D_t/c)} \tag{23c}$$

The operator, L^+, is similarly defined except for a " + " sign before the radical.

Engquist and Majda [17] showed that at a grid boundary, say at $x = 0$, the application of L^- to the wave function, U, will exactly absorb a plane wave propagating toward the boundary at an arbitrary angle, θ. Thus,

$$L^- U = 0 \tag{24}$$

applied at $x = 0$ functions as an exact analytical RBC which absorbs wave motion from the interior of the spatial domain, Ω. The operator, L^+, performs the same function for a plane wave propagating at an arbitrary angle toward the other x boundary in Fig. 8 at $x = h$. The presence of the radical in (23b) classifies L^- as a pseudo-differential operator that is non-local in both the space and time variables. This is an undesirable characteristic in that it prohibits the direct numerical implementation of (24) as an RBC.

Approximations of the radical in (23b) produce RBC's that can be implemented numerically and are useful in FD-TD simulations. The numerical implementation of an RBC is not exact in that a small amount of reflection does develop as numerical waves pass through the grid boundary. However, it is possible to design an RBC which minimizes the reflection over a range of incident angles. The Mur RBC, used in current FD-TD electromagnetic wave codes, is simply a two-term Taylor series approximation to the radical in (23b), given by [11]

$$\sqrt{1-S^2} \simeq 1 - \frac{1}{2}S^2 \tag{25a}$$

Substituting (25a) into (24), we obtain

$$\left(D_x - \frac{D_t}{c} + \frac{cD_y^2}{2D_t}\right)U = 0 \tag{25b}$$

Multiplying (25b) through by D_t, and identifying the differential operators as partial derivatives, we obtain the following approximate, analytical RBC which can be numerically implemented at the $x = 0$ grid boundary

$$U_{xt} - \frac{1}{c}U_{tt} + \frac{c}{2}U_{yy} = 0 \tag{26}$$

Equation (26) is a very good approximation to the exact RBC of (24) for relatively small values of $S = cD_y/D_t$ which satisfy the Taylor series approximation of (25a). This is equivalent to saying that (26) presents a nearly reflectionless grid truncation for numerical plane wave modes which strike the $x = 0$ grid boundary at small values of the incident angle, θ. Analogous approximate, analytical RBC's can be derived for the other grid boundaries

$$U_{xt} + \frac{1}{c}U_{tt} - \frac{c}{2}U_{yy} = 0, \quad x = h \text{ boundary} \tag{27a}$$

$$U_{yt} - \frac{1}{c}U_{tt} + \frac{c}{2}U_{xx} = 0, \quad y = 0 \text{ boundary} \tag{27b}$$

$$U_{yt} + \frac{1}{c}U_{tt} - \frac{c}{2}U_{xx} = 0, \quad y = h \text{ boundary} \tag{27c}$$

For the FD-TD simulation of the vector Maxwell's equations,the RBC's of (26) and (27) are applied to individual Cartesian components of $\overline{E}$ or $\overline{H}$ that are located at, and tangential to, the grid boundaries.

The derivation of RBC's for the three-dimensional case follows the above development closely. The wave equation, given by

$$U_{xx} + U_{yy} + U_{zz} - \frac{1}{c^2}U_{tt} = 0 \tag{28a}$$

has the associated partial differential operator

$$L \equiv D_x^2 + D_y^2 + D_z^2 - \frac{1}{c^2}D_t^2 \tag{28b}$$

L can be factored in the manner of (23a) to provide an exact radiation boundary operator, L^-, having the same form as that of (23b), but with S given by

$$S = \left[\left(\frac{D_y}{D_t/c}\right)^2 + \left(\frac{D_z}{D_t/c}\right)^2\right]^{\frac{1}{2}} \tag{28c}$$

Again, L^- applied to the scalar wave function, U, at the $x = 0$ grid boundary will exactly absorb a plane wave propagating toward the boundary at an arbitrary angle.

Using the Taylor series approximation of (25a), we obtain an approximate RBC at $x = 0$ in differential-operator form

$$\left(D_x - \frac{D_t}{c} + \frac{cD_y^2}{2D_t} + \frac{cD_z^2}{2D_t}\right)U = 0 \tag{29}$$

Multiplying (29) through by D_t, and identifying the differential operators as partial derivatives, we obtain the corresponding approximate, analytical RBC which can be numerically implemented at the $x = 0$ lattice boundary

$$U_{xt} - \frac{1}{c}U_{tt} + \frac{c}{2}U_{yy} + \frac{c}{2}U_{zz} = 0 \tag{30}$$

Equation (30) is a very good approximation of the exact RBC of (24) for relatively small values of S given by (28c). This is equivalent to saying that (30) presents a nearly reflectionless lattice truncation for numerical plane wave modes which strike the $x = 0$ lattice boundary close to broadside. Analogous approximate, analytical RBC's can be derived for the other lattice boundaries:

$$U_{xt} + \frac{1}{c}U_{tt} - \frac{c}{2}U_{yy} - \frac{c}{2}U_{zz} = 0, \quad x = h \text{ boundary} \tag{31a}$$

$$U_{yt} - \frac{1}{c}U_{tt} + \frac{c}{2}U_{xx} + \frac{c}{2}U_{zz} = 0, \quad y = 0 \text{ boundary} \tag{31b}$$

$$U_{yt} + \frac{1}{c}U_{tt} - \frac{c}{2}U_{xx} - \frac{c}{2}U_{zz} = 0, \quad y = h \text{ boundary} \tag{31c}$$

$$U_{zt} - \frac{1}{c}U_{tt} + \frac{c}{2}U_{xx} + \frac{c}{2}U_{yy} = 0, \quad z = 0 \text{ boundary} \tag{31d}$$

$$U_{zt} + \frac{1}{c}U_{tt} - \frac{c}{2}U_{xx} - \frac{c}{2}U_{yy} = 0, \quad z = h \text{ boundary} \tag{31e}$$

For the FD-TD simulation of the vector Maxwell's equations, the RBC's of (30) and (31) are applied to individual Cartesian components of $\overline{E}$ or $\overline{H}$ that are located at, and tangential to, the lattice boundaries.

Equations (26) and (27), representing approximate RBC's for a two-dimensional grid, and (30) and (31), representing approximate RBC's for a three-dimensional lattice, have been found to be very effective when implemented using the differencing scheme proposed by Mur (discussed below). These RBC's truncate an FD-TD space grid or lattice with an overall level of spurious reflections of only 1%–5% for arbitrary targets, if the outer grid or lattice planes are located 10–20 space cells from the target surface. This level of suppression of spurious reflections has been found sufficient to permit highly accurate computational modeling of scattering. For example, the radar cross section of three-dimensional targets spanning 9 wavelengths (96 space cells) has been modeled with an accuracy of 1 dB over a 40-dB dynamic range using an FD-TD space lattice having outer planes located only 0.75 wavelength (8 cells) from the target surface, as is shown in section 8.7.

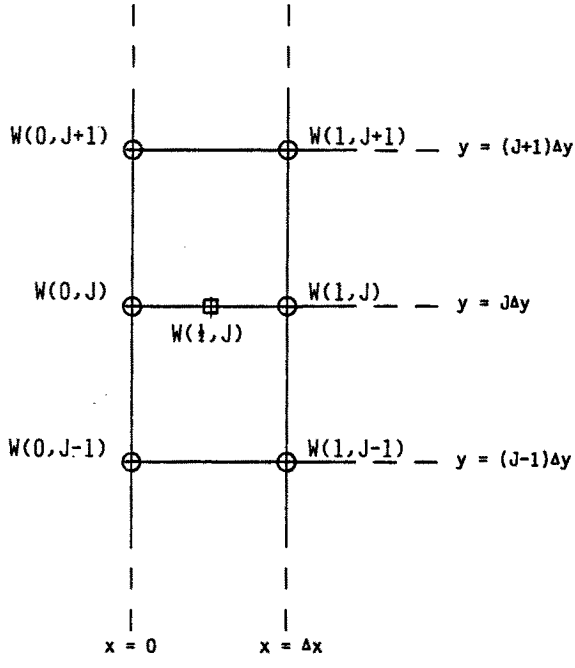

Figure 9 Points near the x=0 boundary used in the Mur differencing scheme.

c. Mur Differencing Scheme

A simple and successful finite-difference scheme for the two-term Taylor series RBC's of (26), (27) and (30), (31) was introduced by Mur [11]. For clarity, this scheme is illustrated for the two-dimensional grid case at the $x = 0$ grid boundary. Referring to Fig. 9, $W^n(i,j)$ represents an individual Cartesian component of $\overline{E}$ or $\overline{H}$ that is located at, and tangential to, the grid boundary at $x = 0$. The Mur scheme involves implementing the partial derivatives of (26) as numerical central differences expanded about the auxiliary W component, $W^n(\frac{1}{2},j)$, located one-half space cell from the grid boundary at $(0,j)$. In the first step of the derivation of the Mur scheme, the mixed partial x and t derivatives on the left hand side of (26) are written out using central differences

$$W_{xt}\Big|_{(\frac{1}{2},j,n)} = \frac{\frac{\partial W^{n+1}}{\partial x}(\frac{1}{2},j) - \frac{\partial W^{n-1}}{\partial x}(\frac{1}{2},j)}{2\Delta t} \tag{32a}$$

$$= \frac{\left[\frac{W^{n+1}(1,j)-W^{n+1}(0,j)}{\Delta x}\right] - \left[\frac{W^{n-1}(1,j)-W^{n-1}(0,j)}{\Delta x}\right]}{2\Delta t}$$

Next, the partial t derivative on the left hand side of (26) is written out as an average of time derivatives at the adjacent points $(0,j)$ and $(1,j)$

$$W_{tt}\Big|_{(\frac{1}{2},j,n)} = \frac{1}{2}\left[\frac{\partial^2 W^n}{\partial t^2}(0,j) + \frac{\partial^2 W^n}{\partial t^2}(1,j)\right]$$

$$= \frac{1}{2}\left[\frac{W^{n+1}(0,j) - 2W^n(0,j) + W^{n-1}(0,j)}{\Delta t^2}\right. \tag{32b}$$

$$\left. + \frac{W^{n+1}(i,j) - 2W^n(1,j) + W^{n-1}(1,j)}{\Delta t^2}\right]$$

And, the partial y derivative on the left hand side of (26) is written out as an average of y derivatives at the adjacent points $(0,j)$ and $(1,j)$

$$W_{yy}\Big|_{(\frac{1}{2},j,n)} = \frac{1}{2}\left[\frac{\partial^2 W^n}{\partial y^2}(0,j) + \frac{\partial^2 W^n}{\partial y^2}(1,j)\right]$$

$$= \frac{1}{2}\left[\frac{W^n(0,j+1) - 2W^n(0,j) + W^n(0,j-1)}{\Delta y^2}\right. \tag{32c}$$

$$\left. + \frac{W^n(1,j+1) - 2W^n(1,j) + W^n(1,j-1)}{\Delta y^2}\right]$$

Substituting the finite-difference expressions of (32) into (26) and solving for $W^{n+1}(0,j)$, we obtain the following time-stepping algorithm for components of W along the $x = 0$ grid boundary which implements the Taylor series RBC of (26)

$$W^{n+1}(0,j) = -W^{n-1}(1,j) + \frac{c\Delta t - \Delta x}{c\Delta t + \Delta x}[W^{n+1}(1,j) + W^{n-1}(0,j)]$$

$$+ \frac{2\Delta x}{c\Delta t + \Delta x}[W^n(0,j) + W^n(1,j)]$$

$$+ \frac{(c\Delta t)^2 \Delta x}{2\Delta y^2 (c\Delta t + \Delta x)}[W^n(0,j+1) - 2W^n(0,j) + W^n(0,j-1)$$

$$+ W^n(1,j+1) - 2W^n(1,j) + W^n(1,j-1)] \tag{33}$$

For a square grid, $\Delta x = \Delta y = \delta$, and the Mur RBC at x = 0 can be written as

$$W^{n+1}(0,j) = -W^{n-1}(1,j) + \frac{c\Delta t - \delta}{c\Delta t + \delta}[W^{n+1}(1,j) + W^{n-1}(0,j)]$$

$$+ \frac{2\delta}{c\Delta t + \delta}[W^n(0,j) + W^n(1,j)]$$

$$+ \frac{(c\Delta t)^2}{2\delta(c\Delta t + \delta)}[W^n(0,j+1) - 2W^n(0,j) + W^n(0,j-1)$$

$$+ W^n(1,j+1) - 2W^n(1,j) + W^n(1,j-1)] \tag{34}$$

Analogous finite-difference expressions for the Mur RBC at each of the other grid boundaries, $x = h, y = 0$, and $y = h$, can be derived by substituting into (27a), (27b), and (27c), respectively, in the same manner. More simply, these Mur RBC's can be obtained by inspection from (33) and (34) using coordinate symmetry arguments.

The derivation of Mur finite-difference expressions for the radiation boundary condition in three dimensions follows the above development closely. For clarity, the Mur scheme is again illustrated at the $x = 0$ lattice boundary, with Fig. 9 now representing individual Cartesian components of $\overline{E}$ or $\overline{H}$ located in lattice plane $z = k\Delta z$. Here, the Mur scheme involves implementing the partial derivatives of (30) as numerical central differences expanded about the auxiliary W component, $W^n(\frac{1}{2}, j, k)$, located one-half space cell from the grid boundary at $(0, j, k)$. The partial derivatives, W_{xt}, W_{tt}, and W_{yy} are identical in form to (32a), (32b), and (32c), respectively, and are evaluated in lattice plane $z = k\Delta z$. The partial derivative, W_{zz}, is expressed as an average of z derivatives at the adjacent points $(0, j, k)$ and $(1, j, k)$

$$
\begin{aligned}
W_{zz}\Big|_{(\frac{1}{2},j,k,n)} &= \frac{1}{2}\left[\frac{\partial^2 W^n}{\partial z^2}(0,j,k) + \frac{\partial^2 W^n}{\partial z^2}(1,j,k)\right] \\
&= \frac{1}{2}\left[\frac{W^n(0,j,k+1) - 2W^n(0,j,k) + W^n(0,j,k-1)}{\Delta z^2}\right. \\
&\quad \left. + \frac{W^n(1,j,k+1) - 2W^n(1,j,k) + W^n(1,j,k-1)}{\Delta z^2}\right]
\end{aligned}
\tag{35}
$$

Substituting these finite-difference expressions into (30) and solving for $W^{n+1}(0, j, k)$, we obtain the following time-stepping algorithm for components of W along the $x = 0$ lattice boundary which implements the Taylor series RBC of (30)

$$W^{n+1}(0,j,k) = -W^{n-1}(1,j,k) + \frac{c\Delta t - \Delta x}{c\Delta t + \Delta x}[W^{n+1}(1,j,k)$$

$$+ W^{n-1}(0,j,k)] + \frac{2\Delta x}{c\Delta t + \Delta x}[W^n(0,j,k) + W^n(1,j,k)]$$

$$+ \frac{(c\Delta t)^2 \Delta x}{2\Delta y^2 (c\Delta t + \Delta x)}[W^n(0,j+1,k) - 2W^n(0,j,k) + W^n(0,j-1,k)$$

$$+ W^n(1,j+1,k) - 2W^n(1,j,k) + W^n(1,j-1,k)]$$

$$+ \frac{(c\Delta t)^2 \Delta x}{2\Delta z^2 (c\Delta t + \Delta x)}[W^n(0,j,k+1) - 2W^n(0,j,k) + W^n(0,j,k-1)$$

$$+ W^n(1,j,k+1) - 2W^n(1,j,k) + W^n(1,j,k-1)] \tag{36}$$

For a cubic lattice, $\Delta x = \Delta y = \Delta z = \delta$, and the Mur RBC at $x = 0$ can be written as

$$W^{n+1}(0,j,k) = -W^{n-1}(1,j,k) + \frac{c\Delta t - \delta}{c\Delta t + \delta}[W^{n+1}(1,j,k)$$

$$+ W^{n-1}(0,j,k)] + \frac{2\delta}{c\Delta t + \delta}[W^n(0,j,k) + W^n(1,j,k)]$$

$$+ \frac{(c\Delta t)^2}{2\delta (c\Delta t + \delta)}[W^n(0,j+1,k) - 4W^n(0,j,k) + W^n(0,j-1,k)$$

$$+ W^n(1,j+1,k) - 4W^n(1,j,k) + W^n(1,j-1,k) + W^n(0,j,k+1)$$

$$+ W^n(0,j,k-1) + W^n(1,j,k+1) + W^n(1,j,k-1)] \tag{37}$$

Analogous finite-difference expressions for the Mur RBC at each of the other lattice boundaries, $x = h, y = 0, y = h, z = 0$, and $z = h$, can

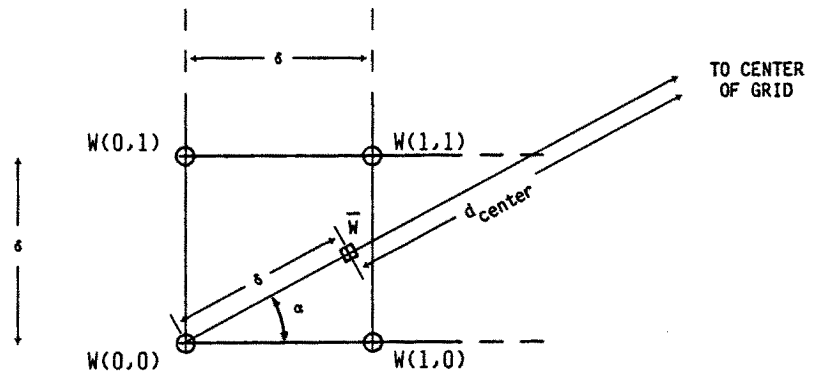

Figure 10 Points near the $x = 0$, $y = 0$ grid corner used in the special corner radiation boundary condition (square grid case).

be derived by substituting into (31a)–(31e), respectively, in the same manner. More simply, these Mur RBC's can be obtained by inspection from (36) and (37) using coordinate symmetry arguments.

d. Special Corner RBC

Upon inspecting (33) and (36), it is clear that the Mur finite-difference scheme for the two-term Taylor series RBC's cannot be implemented for field components located at grid corners, since some of the necessary field data used in the Mur expressions at these points is outside of the grid and not available. It is necessary to implement a special corner radiation boundary condition at these points which: (1) utilizes available field data in the grid; (2) yields acceptably low levels of reflection of outgoing numerical wave modes; and (3) is numerically stable.

Figure 10 illustrates the two-dimensional grid geometry for a simple and stable special corner RBC used successfully since 1982 for a wide variety of two- and three-dimensional FD-TD simulations beginning with that of [12]. The special corner RBC uses a first-order accurate propagation argument wherein the value of a corner field component, for example $W(0,0)$, is taken to be just the time-retarded value of an interior field, $\overline{W}$, located along a radial line connecting the corner point to the center of the grid. This propagation argument

assumes that each scattered numerical wave mode is radially outgoing at the corner point. For simplicity, we further assume that the relation $c\Delta t = \delta/2$ is maintained, so that if $\overline{W}$ is located exactly one cell-width, δ, inward along the radial line, the time retardation of the outgoing numerical wave in propagating from $\overline{W}$ to $W(0,0)$ is exactly two time steps. Overall, the special corner RBC is given by

$$W^{n+1}(0,0) = f_{\text{radial}} \cdot \overline{W}^{n-1} \tag{38}$$

where f_{radial} is the attenuation factor for the radially outgoing wave. In two dimensions, we have from Fig. 10

$$f_{\text{radial}} = \left(\frac{d_{\text{center}}}{d_{\text{center}} + 1}\right)^{\frac{1}{2}} \tag{39a}$$

$$\begin{aligned} \overline{W}^{n-1} = {} & (1 - \sin\alpha)(1 - \cos\alpha)\, W^{n-1}(0,0) \\ & + (1 - \sin\alpha)\cos\alpha\, W^{n-1}(1,0) \\ & + \sin\alpha(1 - \cos\alpha)\, W^{n-1}(0,1) \\ & + \sin\alpha\,\cos\alpha\, W^{n-1}(1,1) \end{aligned} \tag{39b}$$

where d_{center} is the radial distance, in cell-widths, from $\overline{W}$ to the center of the grid, and α is the azimuth angle of the radial line at $W(0,0)$. Note that the value of $\overline{W}^{n-1}$ is determined by simple linear interpolation of the four surrounding field values, including $W(0,0)$, at time step $n-1$. Extension to three dimensions is straightforward, yielding for $W^{n+1}(0,0,k)$

$$f_{\text{radial}} = \left(\frac{d_{\text{center}}}{d_{\text{center}} + 1}\right) \tag{40a}$$

$$\begin{aligned}\overline{W}^{n-1} &= (1-\sin\beta)(1-\cos\beta\sin\alpha)(1-\cos\beta\cos\alpha)\overline{W}^{n-1}(0,0,k)\\ &+(1-\sin\beta)(1-\cos\beta\sin\alpha)\cos\beta\cos\alpha\,\overline{W}^{n-1}(1,0,k)\\ &+(1-\sin\beta)\cos\beta\sin\alpha(1-\cos\beta\cos\alpha)\overline{W}^{n-1}(0,1,k)\\ &+(1-\sin\beta)\cos^2\beta\sin\alpha\cos\alpha\,\overline{W}^{n-1}(1,1,k)\\ &+\sin\beta(1-\cos\beta\sin\alpha)(1-\cos\beta\cos\alpha)\overline{W}^{n-1}(0,0,k+1)\\ &+\sin\beta(1-\cos\beta\sin\alpha)\cos\beta\cos\alpha\,\overline{W}^{n-1}(1,0,k+1)\\ &+\sin\beta\cos\beta\sin\alpha(1-\cos\beta\cos\alpha)\overline{W}^{n-1}(0,1,k+1)\\ &+\sin\beta\cos^2\beta\sin\alpha\cos\alpha\,\overline{W}^{n-1}(1,1,k+1)\end{aligned} \tag{40b}$$

where β is the elevation angle of the radial line at $W(0,0,k)$. Here, note that the value of $\overline{W}^{n-1}$ is determined by simple linear interpolation of the eight surrounding field values, including $W(0,0,k)$, at time step $n-1$. Special RBC's for field components along the other corners of a three-dimensional lattice can be obtained by inspection from (40) using coordinate symmetry arguments, and properly defining angles α and β.

e. *Generalized and Higher-Order RBC's*

Trefethen and Halpern [18] proposed a generalization of the two-term Taylor series approximation to the radical in (23b), considering the use of the rational function approximation

$$\sqrt{1-S^2} \simeq r(S) = \frac{p_m(S)}{q_n(S)} \tag{41}$$

on the interval $[-1,1]$, where p_m and q_n are polynomials in S of degree m and n, respectively; and $r(S)$ is said to be of type (m,n). With $S = cD_y/D_t$, the $[-1,1]$ approximation interval on S is equivalent to approximation of the exact one-way wave equation of (24) along the $x = 0$ grid boundary for the range of incident wave angles $\theta = -90°$ to $\theta = +90°$.

For example, by specifying $r(S)$ as a general (2,0) approximant, the radical is approximated by an interpolating polynomial of the form

$$\sqrt{1-S^2} \simeq p_0 + p_2 S^2 \tag{42a}$$

resulting in the general second-order, approximate, analytical RBC,

$$U_{xt} - \frac{p_0}{c} U_{tt} - p_2 c\, U_{yy} = 0 \tag{42b}$$

The choice of the coefficients, p_0 and p_2, is determined by the method of interpolation that is used. Standard techniques such as Padé, least-square, or Chebyshev approximation are applied with the goal of interpolating the radical optimally over the $[-1,1]$ range of S, thereby producing an approximate RBC whose performance is good over a wide range of incident wave angles. Mur's two-term Taylor series approximation of (25a) is now seen in a more general sense as a Padé (2,0) interpolant, i.e., with coefficients $p_0 = +1$ and $p_2 = -\frac{1}{2}$ in (42b).

Higher-order rational function approximations to the $\sqrt{1-S^2}$ term were proposed in [18] as a means to derive an approximate RBC having good accuracy over a wider range of incident wave angles than that possible with (42). For example, the use of the general type (2,2) rational function

$$\sqrt{1-S^2} \simeq \frac{p_0 + p_2 S^2}{q_0 + q_2 S^2} \tag{43a}$$

gives the general third-order, approximate, analytical RBC

$$q_0\, U_{xtt} + q_2 c^2\, U_{xyy} - \frac{p_0}{c}\, U_{ttt} - p_2 c\, U_{tyy} = 0 \tag{43b}$$

Appropriate selection of the p and q coefficients in (43) produces various families of RBC's, as suggested in [18]. For example, $q_0 = p_0 = 1, p_2 = -\frac{3}{4}$, and $q_2 = -\frac{1}{4}$ gives a Padé (2,2) approximation in (43a) with the resulting RBC functioning better than (26) for numerical waves impacting the $x = 0$ grid boundary at all angles. Figure 11 depicts two ways of quantifying the improved performance of the Padé (2,2) RBC relative to Mur's Padé (2,0) condition [19,20]. In Fig. 11(a), the theoretical numerical wave reflection coefficient is plotted as a function of angle of incidence for the two Padé RBC's. In Fig. 11(b), the total squared-error in a test grid due to imperfect RBC's (generated by a smooth, finite-duration, cylindrical outgoing pulse centered in the grid) is plotted as a function of time-step number for the two RBC's. We see that the theoretical improvement of reflection coefficient for the Padé (2,2) RBC (most pronounced near normal incidence, 0°) translates to about a 10:1 actual reduction of total error energy in the test grid as the outgoing pulse propagates radially through the Cartesian grid

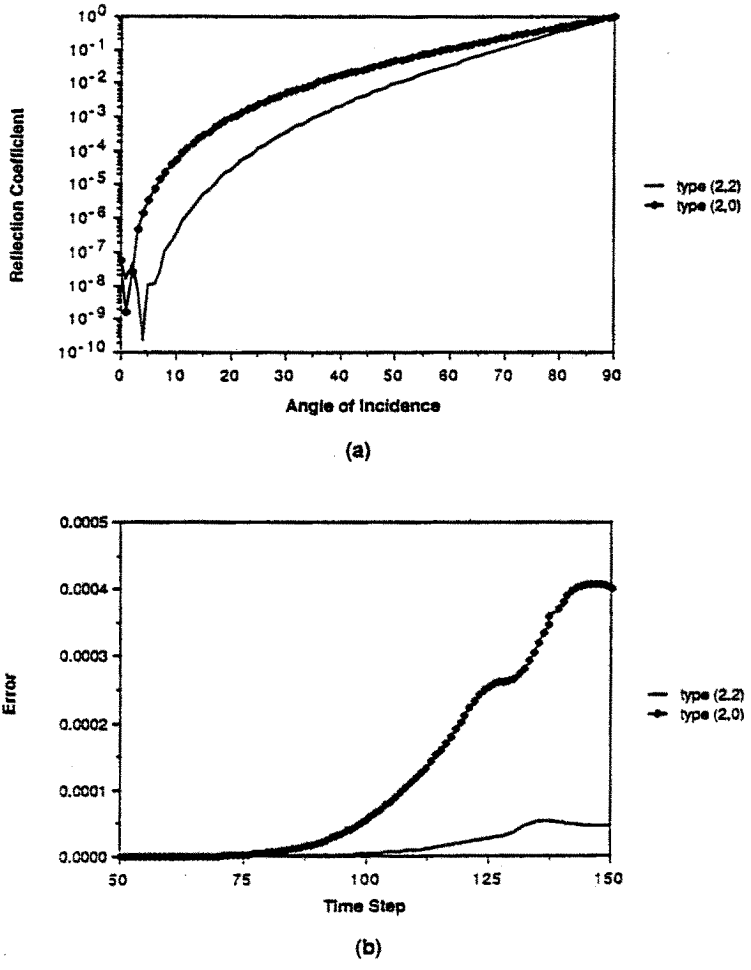

Figure 11 Improved performance of the Padé (2,2) RBC relative to the Mur condition: (a) Theoretical reflection coefficient; (b) Total squared-error in a test grid [19,20].

boundaries. This reduction in grid noise is worthwhile, permitting in principle extension of FD-TD modeling to targets having correspondingly reduced radar cross section. As a consequence, the Padé (2,2) RBC and similar higher-order conditions are currently being studied as potential replacements for the long-used Mur RBC.

8.6 FD-TD Modeling Validations in 2-D

Analytical and code-to-code validations have been obtained relative to FD-TD modeling of electromagnetic wave scattering for a wide variety of canonical two-dimensional structures. Both convex and reentrant (cavity- type) shapes have been studied; and structure material compositions have included perfect conductors, homogeneous and inhomogeneous lossy dielectrics, and anisotropic dielectric and permeable media. Selected validations will be reviewed here.

a. Square Metal Cylinder, TM Polarization

Here, we consider the scattering of a TM-polarized plane wave obliquely incident upon a square metal cylinder of electrical size $k_0 s = 2$, where s is the side width of the cylinder [12]. The square FD-TD grid cell size is set equal to $s/20$, and the grid truncation (radiation boundary) is located at a uniform distance of 20 cells from the cylinder surface.

Figure 12 compares the magnitude and phase of the cylinder surface electric current distribution computed using FD-TD to that computed using a benchmark code which solves the frequency-domain surface electric field integral equation (EFIE) via the method of moments (MOM). The MOM code assumes target symmetry and discretizes one-half of the cylinder surface with 84 divisions. The FD-TD computed surface current is taken as $\hat{n} \times \overline{H}_{\tan}$, where $\hat{n}$ is the unit normal vector at the cylinder surface, and $\overline{H}_{\tan}$ is the FD-TD value of the magnetic field vector component in free space immediately adjacent to the cylinder surface. From Fig. 12, we see that the magnitude of the FD-TD computed surface current agrees with the MOM solution to better than $\pm 1\%$ ($\pm$ 0.09 dB) at all comparison points more than 2 FD-TD cells from the cylinder corners (current singularities). The phase of the FD-TD solution agrees with the MOM solution to within $\pm 3°$ at virtually every comparison point, including the shadow region.

b. Circular Muscle-Fat Layered Cylinder, TE Polarization

Here, we consider the penetration of a TE-polarized plane wave into a simulated biological tissue structure represented by a 15 cm radius muscle-fat layered cylinder [21]. The inner layer (radius = 7.9 cm) is assumed to be comprised of muscle having a relative permittivity of 72 and conductivity of 0.9 S/m. The outer layer is assumed to be

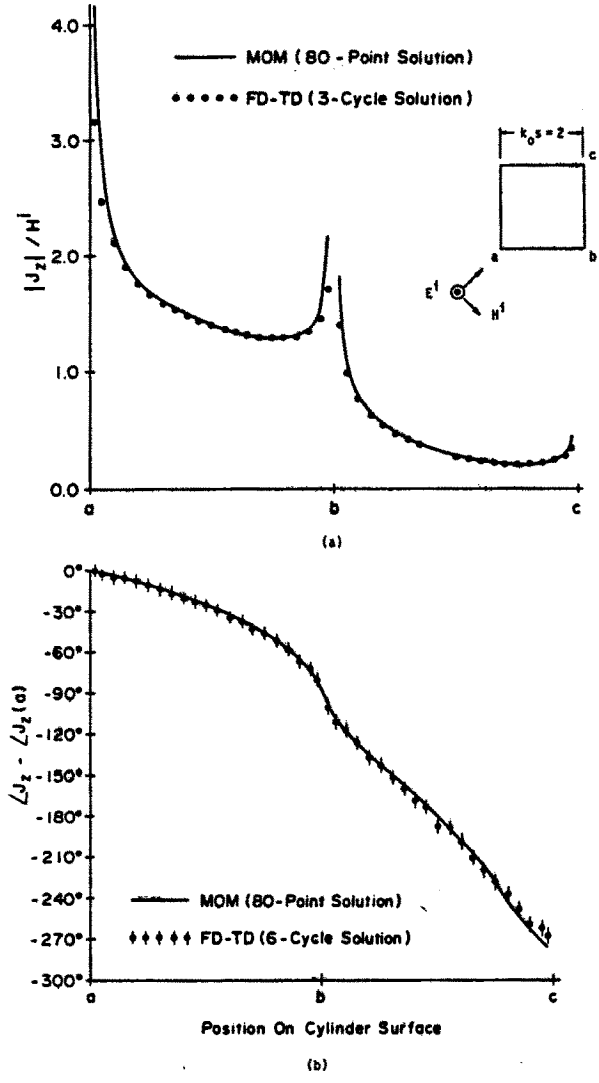

Figure 12 Comparison of FD-TD and MOM results for the cylinder surface electric current distribution: (a) Magnitude; (b) Phase, [12].

comprised of fat having a relative permittivity of 7.5 and conductivity of 0.048 S/m. An illumination frequency of 100 MHz is modeled, with the FD-TD grid cell size set equal to 1.5 cm (approximately 1/24 wavelength within the muscle). A stepped-edge (staircase) approximation of the circular layer boundaries is used.

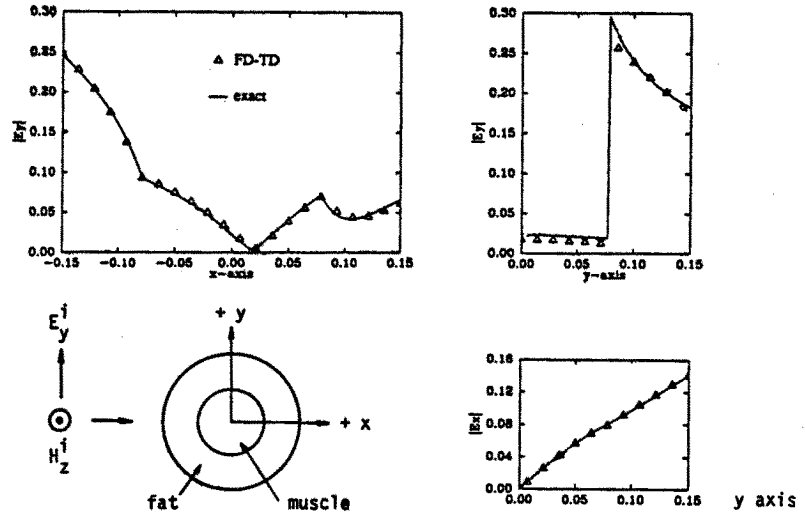

Figure 13 Comparison of FD-TD and exact solution for penetrating electric field vector components within a circular muscle-fat layered cylinder, TE polarization, 100 MHz [21].

Figure 13, taken from [21], shows the analytical validation results for the magnitude of the penetrating electric field vector components along two cuts through the muscle-fat cylinder, one parallel to the direction of propagation of the incident wave, and one parallel to the incident electric field vector. The exact solution is obtained by summing sufficient terms of the eigenfunction expansion to assure convergence of the sum. Excellent agreement of the FD-TD and exact solutions is noted, even at jump discontinuities of the field (and at jump discontinuities of the slope of the field distribution) that occur at the layer boundaries. This fine agreement is observed despite the stepped-edge approximation of the circular layer boundaries.

c. Homogeneous, Anisotropic, Square Material Cylinder

The ability to independently specify electrical permittivity and conductivity for each $\overline{E}$ vector component in the FD-TD lattice, and magnetic permeability and equivalent loss for each $\overline{H}$ vector component, leads immediately to the possibility of using FD-TD to model material structures having diagonalizable tensor electric and magnetic properties [22]. No alteration of the basic FD-TD algorithm is re-

quired. The more complicated behavior associated with off-diagonal tensor components can also be modeled, in principle, with some algorithm complications [23].

Recent development of coupled surface combined-field integral equation (CFIE) theory for modeling electromagnetic wave scattering by arbitrary-shaped, two-dimensional anisotropic material structures [22] has permitted detailed code-to-code validation studies of FD-TD anisotropic models. Figure 14 illustrates one such study. Here, the magnitude of the equivalent surface electric current induced by TM illumination of a square anisotropic cylinder is graphed as a function of position along the cylinder surface for both the FD-TD and CFIE models. The incident wave propagates in the $+y$-direction and has a $+z$-directed electric field. The cylinder has an electrical size $k_0 s = 5$, permittivity $\epsilon_{zz} = 2$, and diagonal permeability tensor $\mu_{xx} = 2$ and $\mu_{yy} = 4$. For the case shown, the FD-TD grid cell size is set equal to s/50, and the radiation boundary is located at a uniform distance of 20 cells from cylinder surface.

From Fig. 14, we see that the FD-TD and CFIE results agree very well almost everywhere on the cylinder surface, despite the presence of a complicated series of peaks and nulls. Disagreement is noted at the cylinder corners where CFIE predicts sharp local peaks, but FD-TD predicts local nulls. Studies are continuing to resolve this corner physics issue.

d. Circular Metal Cylinder, Conformally Modeled

A key flaw in previous FD-TD models of conducting structures with smooth curved surfaces has been the need to use stepped-edge (staircase) approximations of the actual structure surface. Although not a serious problem for modeling wave penetration and scattering for low-Q metal cavities, recent FD-TD studies have shown that stepped approximations of curved walls and aperture surfaces can shift center frequencies of resonant responses by 1% to 2% for Q factors of 30 to 80, and can possibly introduce spurious nulls [16]. In the area of scattering, the use of stepped surfaces has limited application of FD-TD for modeling the important class of targets where surface roughness, exact curvature, and dielectric or permeable loading is important in determining the radar cross section.

Recently, a number of FD-TD conformal surface models have been proposed for two-dimensional problems. These fall into two principal

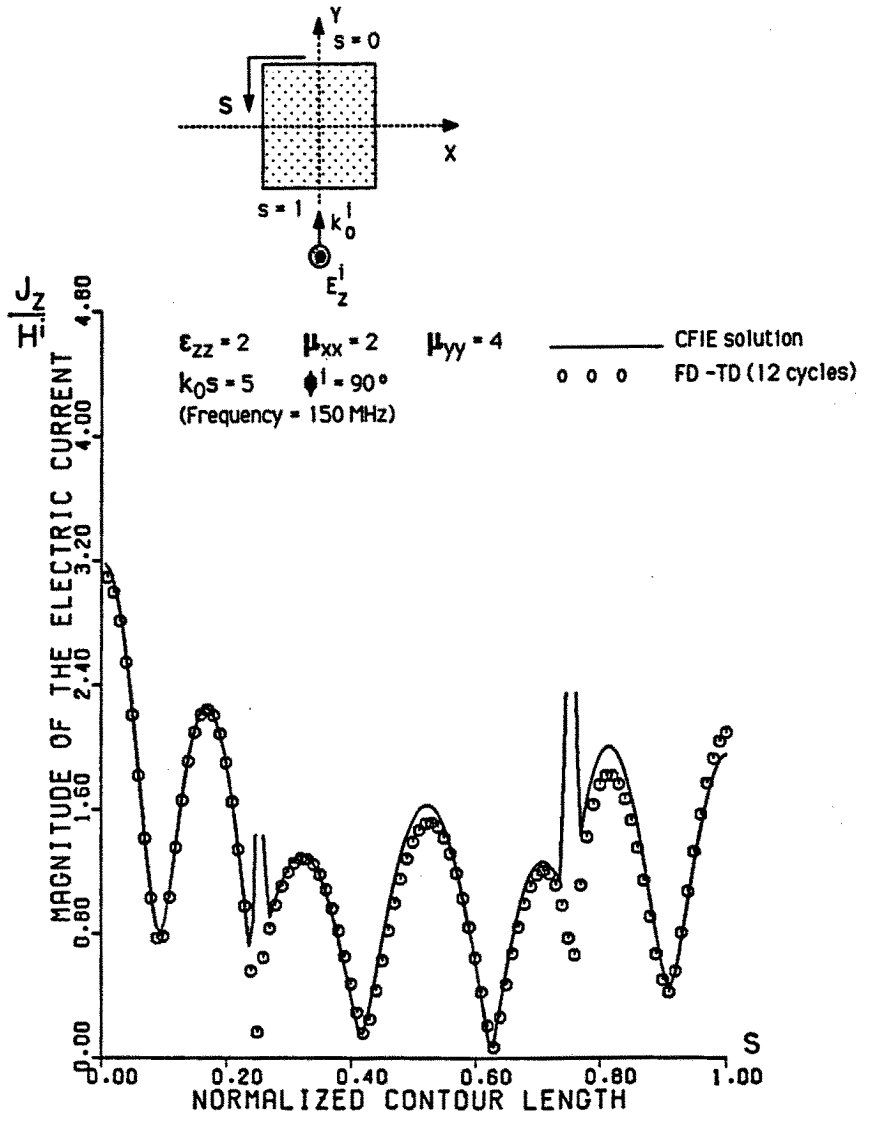

Figure 14 Comparison of FD-TD and CFIE solutions for longitudinal surface electric current on a $k_0 s = 5$ square anisotropic cylinder, TM case [22].

groups:

1. *Locally-stretched grid models.* These preserve the basic Cartesian grid arrangement of field components at all space cells except those adjacent to the structure surface. Space cells adjacent to the surface are deformed to conform with the surface locus. Only field components in these cells are provided with a modified time-stepping algorithm. Examples of this approach include Faraday's Law contour path models [24] and the mixed-polygonal modified finite volume method [25].

2. *Globally-stretched grid models.* These employ available numerical mesh generation schemes to construct non-Cartesian grids which are continuously and globally stretched to conform with structure surfaces. Examples of this approach include Cartesian algorithms adapted for the curvilinear grid case [26], control region algorithms [27], and tangential flux conservation schemes [28].

Research is ongoing for each of these types of conformal surface models. Key questions include: ease of mesh generation; suppression of numerical artifacts such as instability, dispersion, pseudo-refraction, and subtraction noise limitation of computational dynamic range; coding complexity; and computer execution time.

The accuracy of the Faraday's Law contour path models for smoothly curved structures subjected to TE and TM illumination is illustrated in Figs. 15a and 15b, respectively. Here, a moderate-resolution Cartesian FD-TD grid (having 1/20 wavelength cell size) is used to compute the azimuthal or longitudinal electric current distribution on the surface of a $ka = 5$ circular metal cylinder. For both polarizations, the contour path FD-TD model achieves an accuracy of 1.5% or better at most surface points relative to the exact series solution. Running time for the conformal FD-TD model is essentially the same as for the old staircase FD-TD model since only a few H components immediately adjacent to the target surface require a slightly modified time-stepping relation.

e. Flanged Metal Open Cavity

Here, we consider the interactions of a TM-polarized plane wave obliquely incident upon a flanged metal open cavity [29]. The open cavity is formed by a flanged parallel-plate waveguide having a plate spacing, a, of 1m, short-circuited by a terminating plate located at a

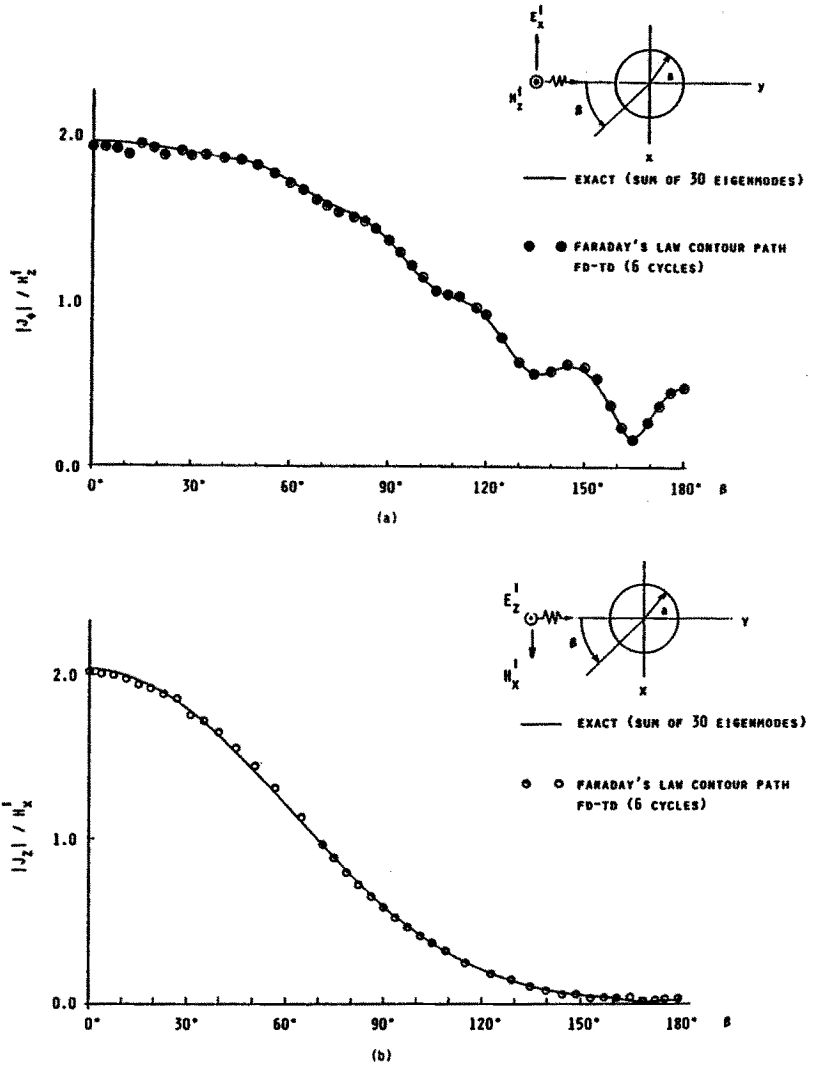

Figure 15 Comparison of FD-TD and exact solution for surface electric current distribution on a $ka = 5$ circular conducting cylinder (conformal FD-TD model used, 0.05 wavelength grid cell size): (a) TE case, azimuthal current; (b) TM case, longitudinal current [24].

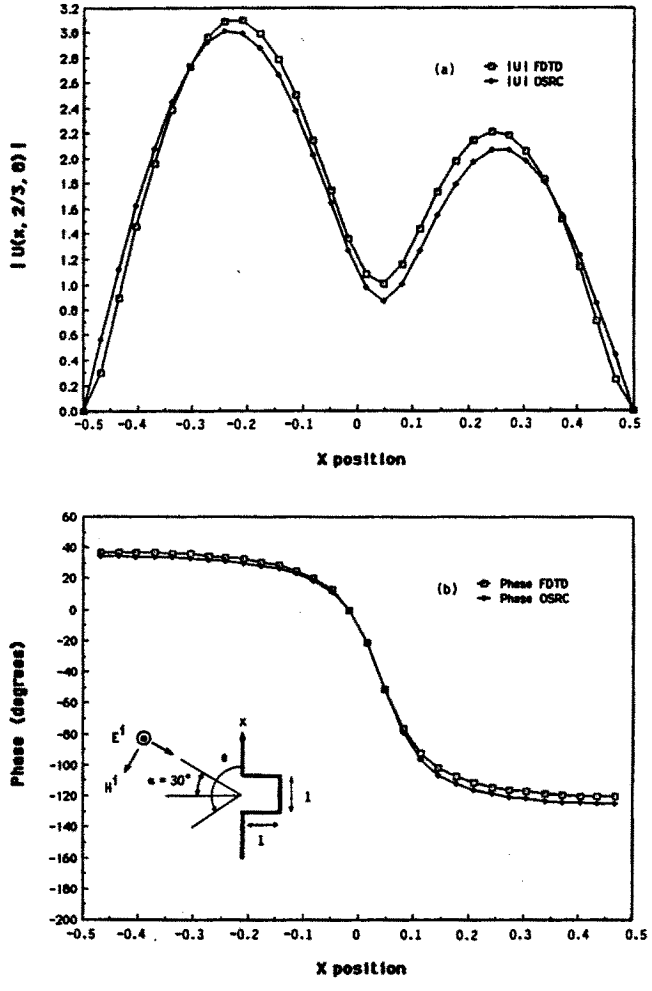

Figure 16 Comparison of FD-TD and modal/OSRC approximate solution for the penetrating electric field distribution 2/3 m within the flanged open cavity: (a) Magnitude; (b) Phase, [29].

distance, d, of 1m from the aperture. At the assumed illumination frequency of 382 MHz, $ka = kd = 8$, and only the first two TE waveguide modes propagate within the open cavity. An oblique angle of incidence, $\alpha = 30°$, is assumed for this case.

Figure 16 compares the magnitude and phase of the penetrating electric field within the cavity 2/3 m from the aperture computed using

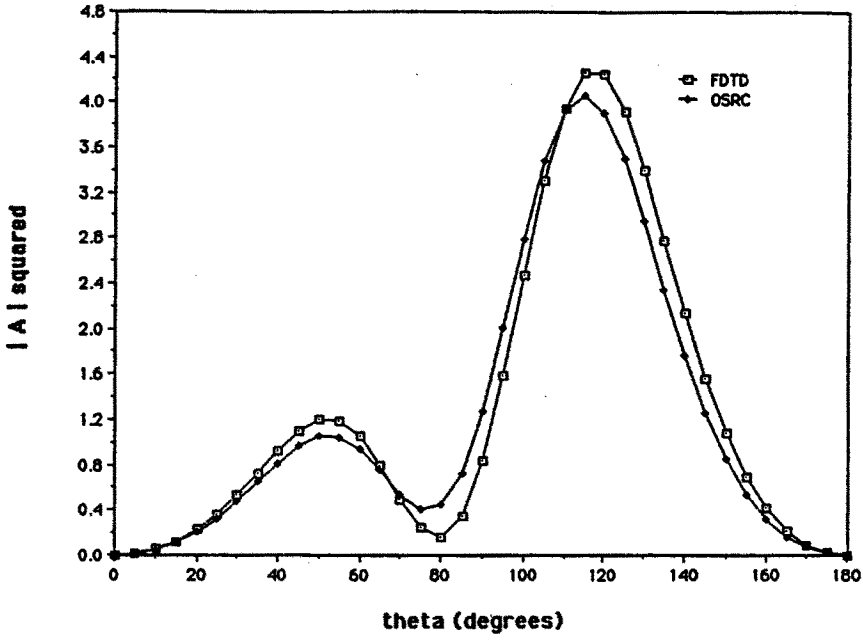

Figure 17 Comparison of FD-TD and modal/OSRC approximate solution for the bistatic radar cross section due to the induced aperture field distribution of the flanged open cavity [29].

FD-TD to that computed using a cavity modal expansion and OSRC [29]. Good agreement is seen. Figure 17 shows a similar comparison for the bistatic radar cross section due to the induced aperture field distribution. Again, good agreement is noted.†

f. Relativistically Vibrating Mirror, Oblique Incidence

Analytical validations have been recently obtained for FD-TD models of reflection of a monochromatic plane wave by a perfectly conducting surface either moving at a uniform relativistic velocity or vibrating at a frequency and amplitude large enough so that the sur-

† It should be noted that the results obtained using the cavity modal expansion and OSRC represent a good approximation, but not a rigorous solution.

face attains relativistic speeds [30,31]. This FD-TD approach is novel in that it does not require a system transformation where the conducting surface is at rest. Instead, the FD-TD grid is at rest in the laboratory frame, and the computed field solution is given directly in the laboratory frame. This is accomplished by implementing the proper relativistic boundary conditions for the fields at the surface of the moving conductor.

Figure 18 shows results for one of the more interesting problems of this type modeled so far, that of oblique plane wave incidence on an infinite vibrating mirror. This case is much more complicated than the normal incidence case in that it has no closed-form solution. An analysis presented in the literature [32] writes the solution in an infinite-series form using plane-wave expansions, where the unknown coefficients in the series are solved numerically. This analysis serves as the basis of comparison for the FD-TD model results for the time variation of the scattered field envelope at points near the mirror.

Since it is difficult to model exactly an infinite plane mirror in a finite two-dimensional grid, a long, thin, rectangular perfectly conducting slab is used as the mirror model, as shown in Fig. 18a. Relativistic boundary conditions for the fields are implemented on the front and back sides of the slab. The other two sides, parallel to the velocity vector, are insensitive to the motion of the slab, and therefore no relativistic boundary conditions are required there. To minimize the effect of edge diffraction, the slab length is carefully selected so that the slab appears to be infinite in extent at observation point, P, during a well-defined early-time response when the edge effect has not yet propagated to P. Since the TM case does not provide appreciably different results than the TE case [32], only the TE case is considered. From Fig. 18b, we see good agreement between the FD-TD and analytical results obtained from [32] for the envelope of the scattered E field vs. time for an incident angle of 30°, peak mirror speed 20% that of light, and observation points $z/d = -5$ and $z/d = -50$, where $kd = 1$ [30]. Similar agreement is shown in [31] for the major propagating sidebands of the reflected field spectrum (at oblique incidence angles up to 50°). This agreement is satisfying since the action of the relativistically vibrating mirror is so complicated, generating a reflected wave having a spread both in frequency and spatial reflection angle, as well as evanescent modes.

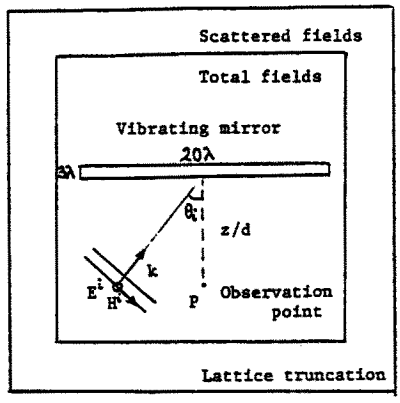

(a)

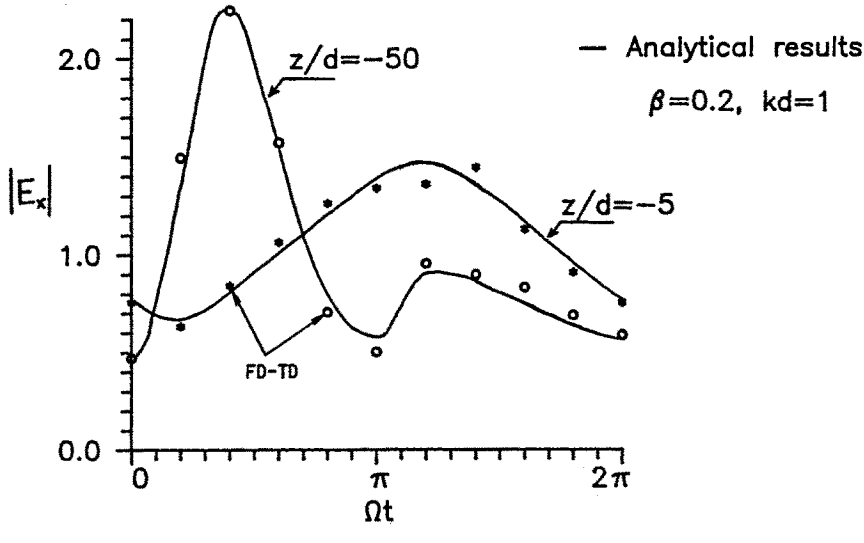

(b)

Figure 18 Comparison of FD-TD and analytical results for the envelope of the scattered E field vs. time for a monochromatic plane wave illuminating a vibrating mirror at 30° [30].

8.7 FD-TD Modeling Validations in 3-D

Analytical, code-to-code, and experimental validations have been obtained relative to FD-TD modeling of electromagnetic wave scattering for a wide variety of canonical three-dimensional structures, including cubes, flat plates, and crossed plates. Selected validations will be reviewed here.

a. Metal Cube, Broadside Incidence

Results are now shown for the FD-TD computed surface electric current distribution on a metal cube subject to plane-wave illumination at broadside incidence [13]. The electric current distribution is compared to that computed by solving a frequency-domain surface EFIE using a standard triangular surface-patching MOM code [13]. It is shown that a very high degree of correspondence exists between the two sets of predictive data.

The detailed surface current study involves a cube of electrical size $k_0 s = 2$, where s is the size width of the cube. For the FD-TD model, each face of the cube is spanned by 400 square cells (20 × 20), and the radiation boundary is located at a uniform distance of 15 cells from the cube surface. For the MOM model, each face of the cube is spanned by either 18 triangular patches or 32 triangular patches (to test the convergence of the MOM model). Comparative results for surface current are graphed along two straight-line loci along the cube: $\overline{abcd}$, which is in the plane of the incident magnetic field; and $\overline{ab'c'd}$, which is in the plane of the incident electric field.

Figure 19 compares the FD-TD and MOM results for the magnitude and phase of the surface current along $\overline{ab'c'd}$. The FD-TD values agree with the high-resolution MOM data to better than ±2.5% (± 0.2 dB) at all comparison points. Phase agreement for the same sets of data is better than ±1°. (The low-resolution MOM data has a phase anomaly in the shadow region.) In Fig. 20, comparably excellent agreement is obtained along $\overline{abcd}$, but only after incorporation of an edge-correction term in the MOM code [33] to enable it to properly model the current singularities at the cube corners, b and c.

b. Flat Conducting Plate, Multiple Monostatic Looks

We next consider a 30 cm × 10 cm × 0.65 cm flat conducting plate target [14], [23]. At 1 GHz, where the plate spans 1 wavelength,

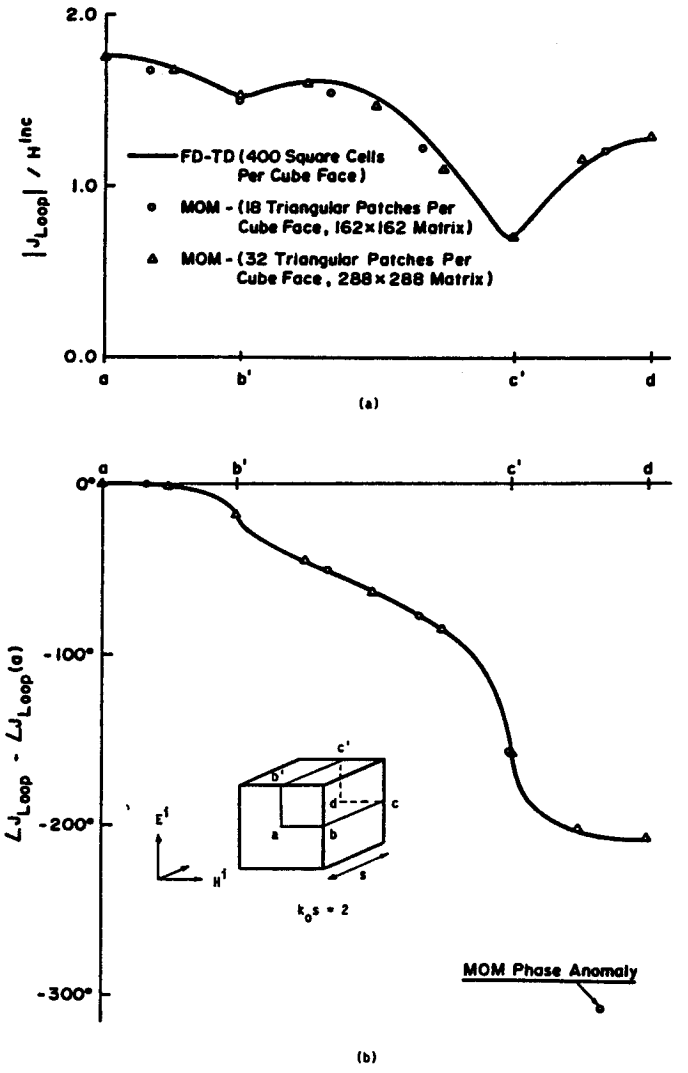

Figure 19 Comparison of FD-TD and MOM results for the cube surface electric current distribution along the E-plane locus, $\overline{ab'c'd}$: (a) Magnitude; (b) Phase, [13].

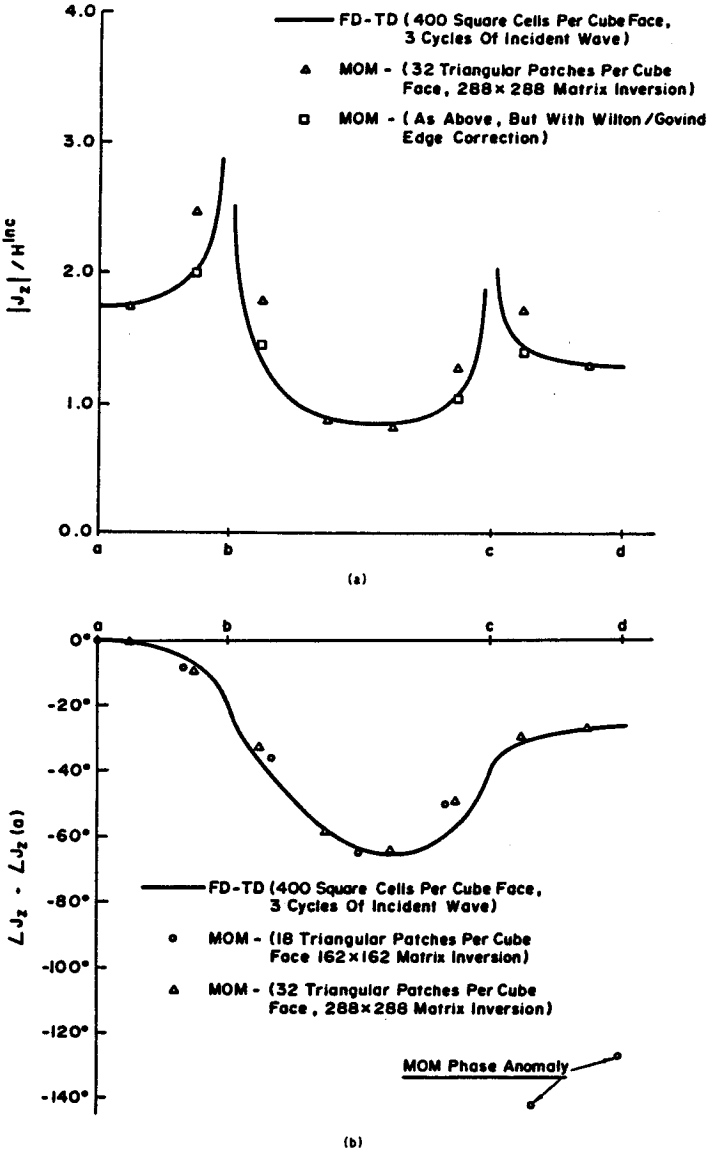

Figure 20 Comparison of FD-TD and MOM results for the cube surface electric current distribution along the n-plane locus, $\overline{abcd}$: (a) Magnitude; (b) Phase.

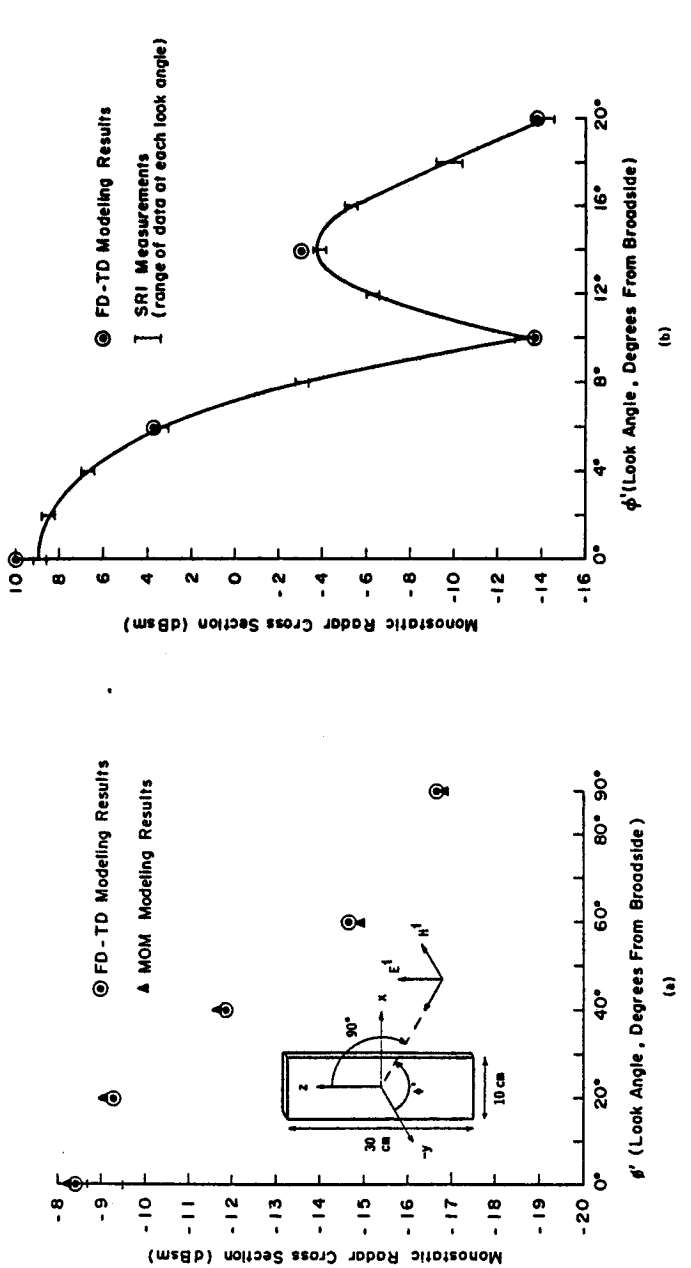

Figure 21 Validation of FD-TD results for the monostatic RCS of a flat conducting plate: (a) Versus MOM at 1 GHz (plate size = 1 λ_0); (b) Versus SRI measurements at 9 GHz (plate size = 9 λ_0) [14,23].

a comparison is made between FD-TD and MOM results for the monostatic radar cross section (RCS) vs look-angle azimuth (keeping a fixed elevation angle), as shown in Fig. 21(a). Here, the FD-TD model uses a uniform cell size of 0.625 cm ($\lambda_0/48$), forming the plate by 48 × 16 × 1 cells. The radiation boundary is located at a uniform distance of only 8 cells from the plate surface. From the MOM model, study of the convergence of the computed broadside RCS indicates that the plate thickness must be accounted by using narrow side patches, and the space resolution of each surface patch should be finer than approximately 0.2 wavelength. As a result, the MOM model forms the plate by 10 × 3 × 1 divisions, yielding a total of 172 triangular surface patches. Figure 21(a) shows excellent agreement between the two models (within about ±0.2 dB).

At 9 GHz, the plate spans 9 wavelengths, and the use of the MOM model is virtually precluded. If we follow the convergence guidelines discussed above, the plate would require approximately 50 × 15 × 1 divisions to properly converge, yielding a total of 3,260 triangular surface patches, and requiring the generation and inversion of a 4,890 × 4,890 complex-valued system matrix. On the other hand, FD-TD remains feasible for the plate at 9 GHz. Choosing a uniform cell size of 0.3125 cm (λ_0/ 10.667), the plate is formed by 96 × 32 × 2 cells. With the radiation boundary again located only 8 cells from the plate surface, the overall lattice size is 112 × 48 × 18, containing 580,608 unknown field components (real numbers). Figure 21b shows excellent agreement between the FD-TD results and measurements of the monostatic RCS vs. look angle performed in the anechoic chamber facility operated by SRI International. The observed agreement is within about 1 dB and 1° of look angle. As will be seen next, this level of agreement is maintained for more complicated targets having corner reflector properties.

c. T-shaped Conducting Target, Multiple Monostatic Looks

We last consider the monostatic RCS pattern of a T-shaped target comprised of two flat conducting plates electrically bonded together [14,23]. The main plate has the dimensions 30 cm × 10 cm × 0.33 cm, and the bisecting fin is 10 cm × 10 cm × 0.33 cm. † The illumination

† The center line of the "bisecting" fin is actually positioned 0.37 cm to the right of the center line of the main plate. This is accounted for in the FD-TD model.

is a 9.0-GHz plane wave at 0° elevation angle and TE polarization relative to the main plate. Thus, the main plate spans 9.0 wavelengths. Note that look-angle azimuths between 90° and 180° provide substantial corner reflector physics, in addition to the edge diffraction, corner diffraction, and other effects found for an isolated flat plate.

For this target, the FD-TD model uses a uniform cell size of 0.3125 cm ($\lambda_0/10.667$), forming the main plate by 32 × 96 × 1 cells and the bisecting fin by 32 × 32 × 1 cells. With the radiation boundary again located only 8 cells from the target's maximum surface extensions, the overall lattice size is 48 × 112 × 48, containing 1,548,288 unknown field components (212.6 cubic wavelengths). Starting with zero-field initial conditions, 661 time steps are used, equivalent to 31 cycles of the incident wave at 9.0 GHz.

Figure 22 compares the FD-TD predicted monostatic RCS values at 32 key look angles between 0° and 180° with measurements performed by SRI International. These look angles are selected to define the major peaks and nulls of the monostatic RCS pattern. It is seen that the agreement is again excellent: in amplitude, within about 1 dB over a total RCS-pattern dynamic range of 40 dB; and in azimuth, within 1° in locating the peaks and nulls of the RCS pattern. Note especially the fine agreement for look-angle azimuths greater than 90°, where there is a pronounced corner reflector effect.

8.8 Penetration and Coupling in 2-D and 3-D

a. *Penetration Models for Narrow Slots and Lapped Joints*

The physics of electromagnetic wave transmission through narrow slots and lapped joints in shielded enclosures must be accurately understood to permit good engineering design of equipment to meet specifications for performance concerning electromagnetic pulse, lightning, high-power microwaves, electromagnetic interference and compatibility, undesired radiated signals, and RCS. In many cases, slots and joints can have very narrow gaps filled by air, oxidation films, or layers of anodization. Joints can be simple (say, two metal sheets butted together); more complex (a lapped or "furniture" joint); or even more complex (a threaded screw-type connection with random points of metal-to-metal contact, depending upon the tightening). Extra complications arise from the possibility of electromagnetic resonances within the joint, either in the transverse or longitudinal (depth) direction.

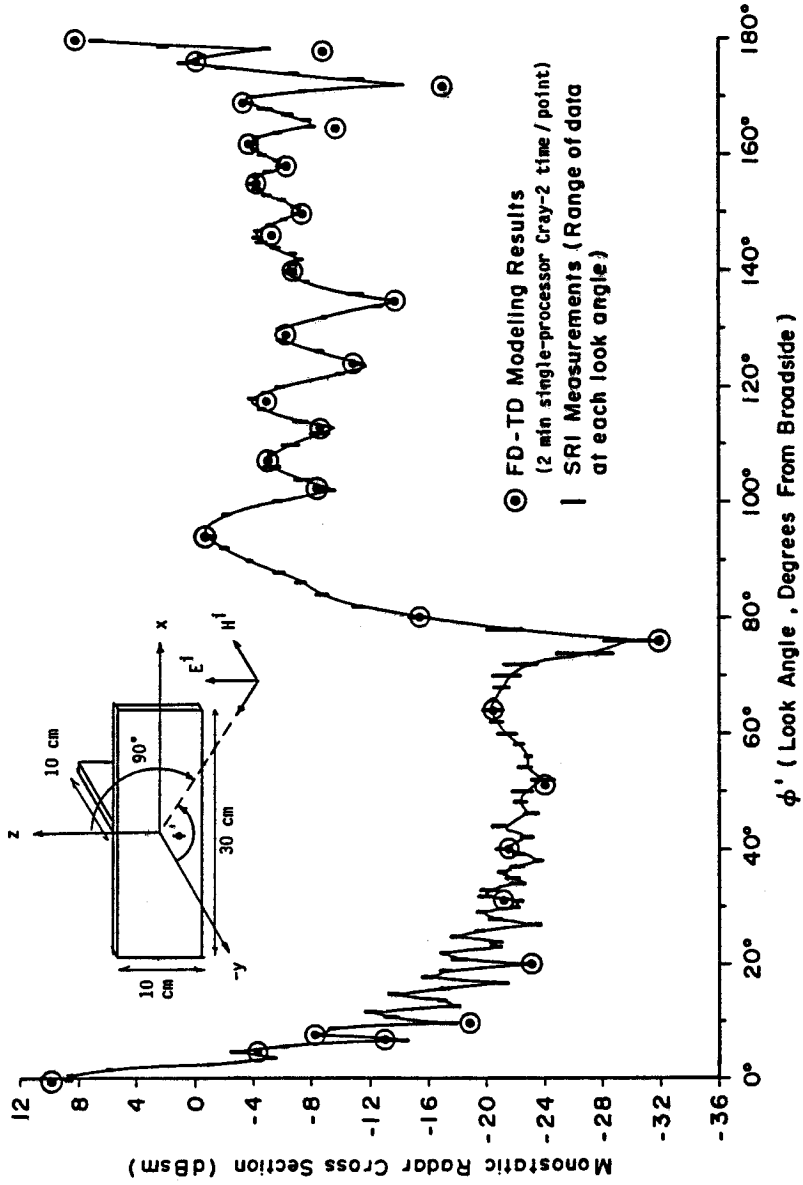

Figure 22 Comparison of FD-TD modeling predictions with SRI measurements of monostatic RCS for the crossed-plate scatterer at 9 GHz (maximum scatterer size = 9 λ_0) [14,23].

Clearly, to make any headway with this complicated group of problems using the FD-TD approach, it is necessary to develop and validate FD-TD models which can simulate the geometric features of generic slots and joints. Since a key geometric feature is likely to be the narrow gap of the slot or joint relative to one FD-TD space cell, it is important to understand how sub-cell gaps can be efficiently modeled.

Three different types of FD-TD sub-cell models have been proposed and examined for modeling narrow slots and joints:

1. *Equivalent slot loading* [34]. Here, rules are set to define an equivalent permittivity and permeability in a slot formed by a single-cell gap to effectively narrow the gap to the desired degree.

2. *Subgridding* [35]. Here, the region within the slot or joint is provided with a sufficiently fine grid. This grid is properly connected to the coarser grid outside of the slot.

3. *Faraday's Law contour path model* [15]. Here, as discussed in section 8.4c, special FD-TD time-stepping relations (based on Faraday's Law in integral form) are implemented for the longitudinal magnetic field components located immediately adjacent to the screen.

The accuracy of the Faraday's Law contour path model for narrow slots and joints is illustrated in Figs. 23–25 by direct comparison of the computed gap electric field distribution against high-resolution numerical benchmarks [15]. Figure 23 models a 0.1 wavelength thick conducting screen which extends 0.5 wavelength to each side of a straight slot which has a gap of 0.025 wavelength. Broadside TE illumination is assumed. Three types of predictive data are compared: (1) The low-resolution (0.1 λ_0) FD-TD model using the contour path approach to treat the slot as a 1/4-cell gap; (2) A high-resolution (0.025 λ_0) FD-TD model treating the slot as a 1-cell gap; and (3) A very-high-resolution frequency-domain EFIE model, solved via MOM (having 0.0025 λ_0 sampling in the slot) which treats the slotted screen as a pure scattering geometry. From Fig. 23, we see that there is excellent agreement between all three sets of predictive data in both magnitude and phase. Of particular interest is the ability of the low-resolution FD-TD model, using the contour path approach, to accurately compute the peak electric field in the slot.

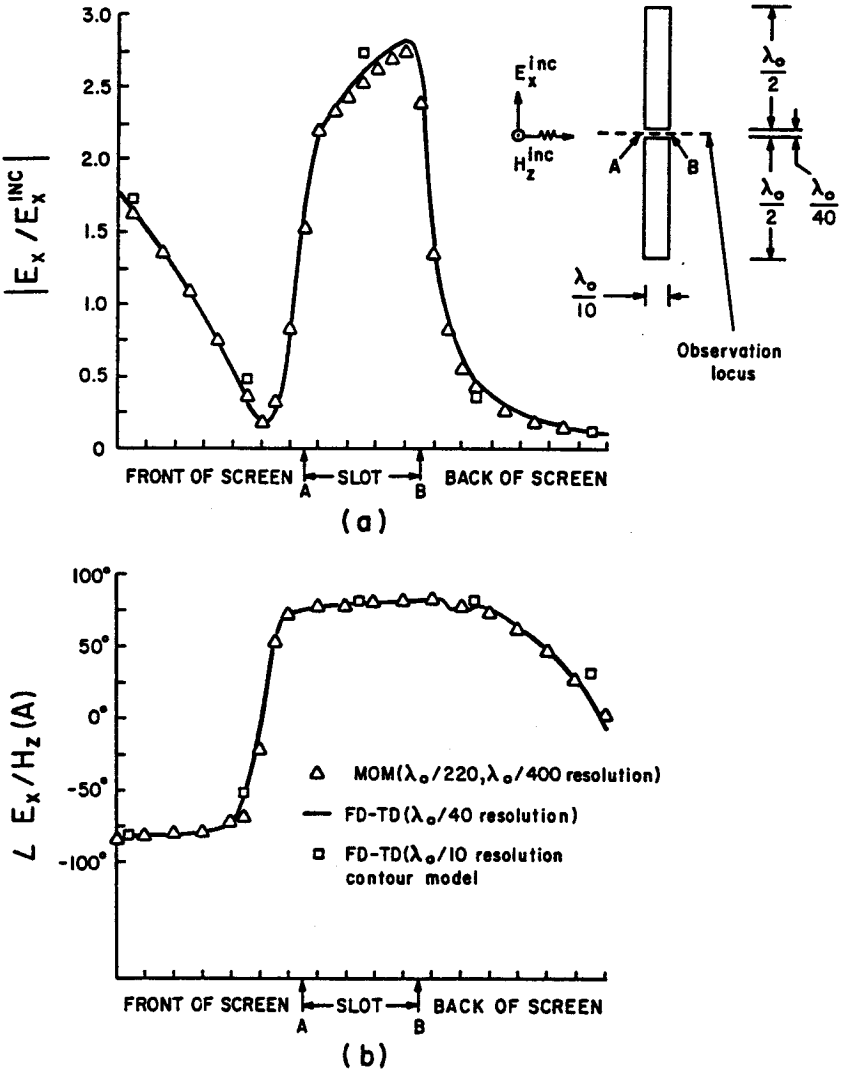

Figure 23 Comparison of FD-TD and MOM solutions for the GAP electric field distribution, straight slot case: (a) Magnitude; (b) Phase.

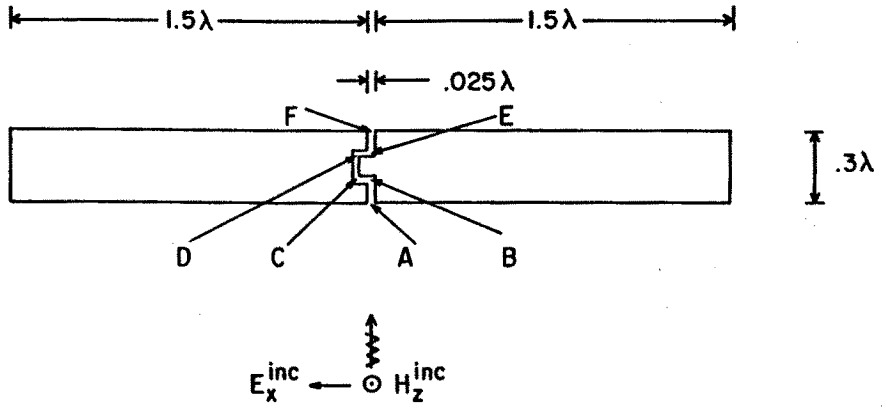

Figure 24 Geometry of U-shaped lapped joint for TE illumination, shown to scale [15].

Figure 24 shows the geometry of a U-shaped lapped joint which was selected for detailed study of path-length (depth) power transmission resonances. The U shape of the joint permits adjustment of the overall joint path length without disturbing the positions of the input and output ports at A and F. A uniform gap of 0.025 wavelength is assumed, as is a screen thickness of 0.3 wavelength and width of 3 wavelengths. Figure 25 compares the gap electric field distribution within the joint as computed by : (1) A low-resolution (0.09 λ_0) contour path FD-TD model treating the gap as 0.28 cell; and (2) A high resolution (0.025 λ_0) FD-TD model treating the gap as 1 cell. The total path length *ABCDEF* within the lapped joint is adjusted to equal 0.45 wavelength, which provides a sharp power transmission peak to the shadow side of the screen. From Fig. 25, we see a very good agreement between the low- and high-resolution FD-TD models, even though this is a numerically stressful resonant penetration case.

An implication of these results is that coarse (0.1 λ_0) FD-TD gridding can be effectively used to model the fine-grained physics of wave penetration through sub-cell slots and joints if simple algorithm modifications are made in accordance with the contour path approach. This can substantially reduce computer resource requirements and coding complexity for FD-TD models of complex structures, without sacrificing appreciable accuracy in the results.

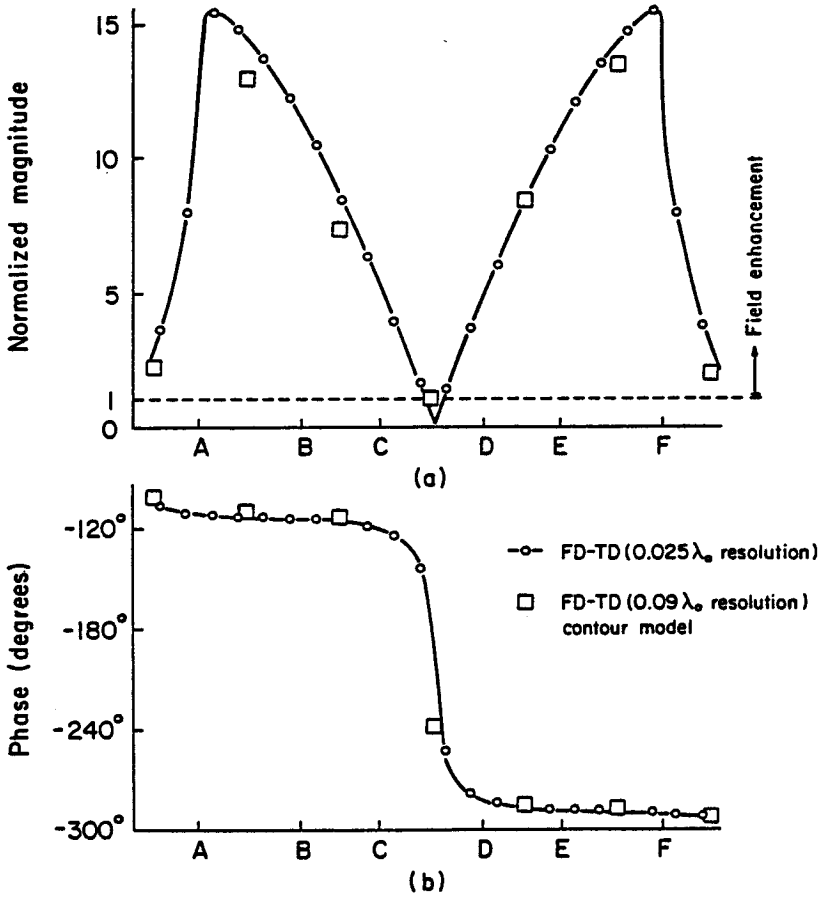

Figure 25 FD-TD computed gap electric field distribution within the lapped joint at the first transmission resonance: (a) $|E_{gap}/E_{inc}|$; (b) $\angle E_{gap}/H_z(A)$ [15].

b. Coupling Models for Wires and Wire Bundles

In equipment design for threats represented by electromagnetic pulse, high-power microwaves, and electromagnetic interference, understanding electromagnetic wave coupling to wires and cable bundles located within shielding enclosures is a problem that is complementary to that of wave penetration through apertures of the shield (such as narrow slots and joints). Similar to the narrow slot problem, a key dimension of the interacting structure, in this case the wire or bundle

diameter, may be small relative to one FD-TD space cell. Thus, it is important to understand how thin sub-cell wires and bundles can be efficiently modeled if FD-TD is to have much application to coupling problems.

Two different types of FD-TD sub-cell models have been proposed and examined for modeling thin wires:

1. *Equivalent inductance* [36]. Here, an equivalent inductance is defined for a wire within a space cell, permitting a lumped-circuit model of the wire to be set up and computed in parallel with the field solution.

2. *Faraday's Law contour path model* [16]. Here, as discussed in section 8.4d, special FD-TD time-stepping relations (based on Faraday's Law in integral form) are implemented for the azimuthal magnetic field components located immediately adjacent to the wire. These relations incorporate assumed $1/r$ singularities of the scattered azimuthal magnetic field and radial electric field adjacent to the wire.

The accuracy of the Faraday's Law contour path model for thin wires in free space is illustrated in Fig. 26 [16]. Figure 26a graphs the scattered azimuthal magnetic field at a fixed distance of 1/20 wavelength from the center of an infinitely long wire having a radius ranging between 1/30,000 and 1/30 wavelength. TM illumination is assumed. We see that there is excellent agreement between the exact series solution and the low-resolution ($0.1\ \lambda_0$) FD-TD contour path model over the entire 3-decade range of wire radius. Figure 26b graphs the scattered azimuthal magnetic field distribution along a 2.0-wavelength (antiresonant) wire of radius 1/300 wavelength. Broadside TM illumination is assumed, and the field is observed at a fixed distance of 1/20 wavelength from the wire center. We see that there is excellent agreement between a frequency-domain EFIE (MOM) solution sampling the wire current at 1/60 wavelength increments, and the low-resolution ($0.1\ \lambda_0$) FD-TD contour path model.

The FD-TD contour path model can be extended to treat thin wire bundles, as well as single wires. Figure 27 shows the code-to-code validation results for the induced currents on a bundle comprised of 4 wires, where 3 are of equal length. Here, a wire of length 60 cm (2.0 wavelengths) is assumed to be at the center of the bundle, and three parallel wires of length 30 cm (1.0 wavelength) are assumed to be located at 120° angular separations on a concentric circle of radius

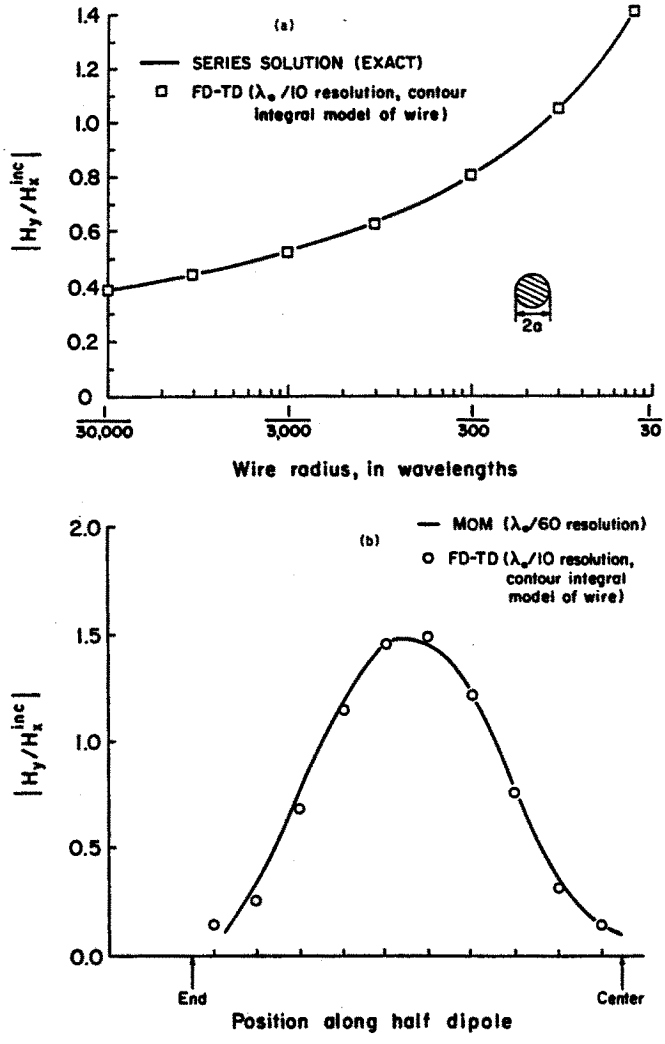

Figure 26 Validation studies for the FD-TD Faraday's Law contour path model for thin wires in free space: (a) Comparison of FD-TD and exact solutions for scattered circumferential magnetic field at point 1/20 wavelength from center of infinite wire; (b) Comparison of FD-TD and MOM solutions for scattered circumferential magnetic field distribution along 2.0-wavelength (antiresonant) wire of radius 1/300 wavelength (broadside TM illumination).

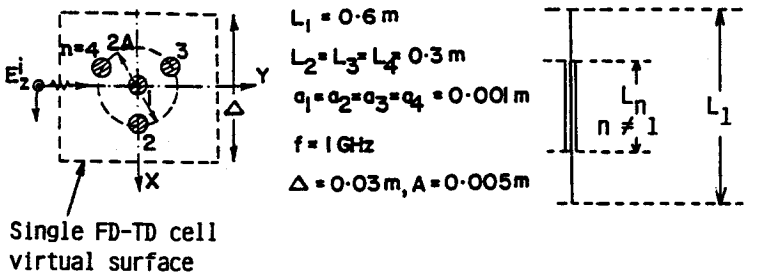

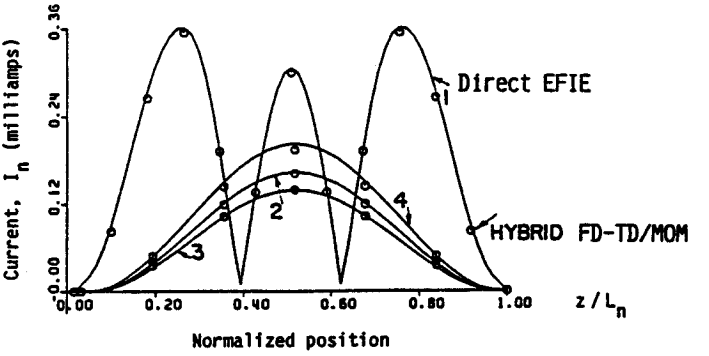

Figure 27 Comparison of hybrid FD-TD/MOM modeling predictions with direct EFIE for induced currents on a wire bundle illuminated broadside by a plane wave in free space [16].

5 mm (1/60 wavelength). The radii of all wires in the bundle are equal and set to 1 mm (1/300 wavelength). The assumed excitation is in free space, provided by a 1-GHz broadside TM plane wave. Following the technique of [16], the bundle is replaced by a single wire having varying equivalent radius corresponding to the three sections along the bundle axis. The physics of the single wire of varying equivalent radius is incorporated in a low-resolution (0.1 λ_0) FD-TD contour path model, as discussed above. The FD-TD model is then run to obtain the tangential E and H fields at a virtual surface conveniently located at the cell boundary containing the equivalent wire (shown as a dashed line in Fig. 27). These fields are then utilized as excitation to obtain the currents induced on the individual wires of the original bundle. This last step is performed by setting up an EFIE and solving via MOM.

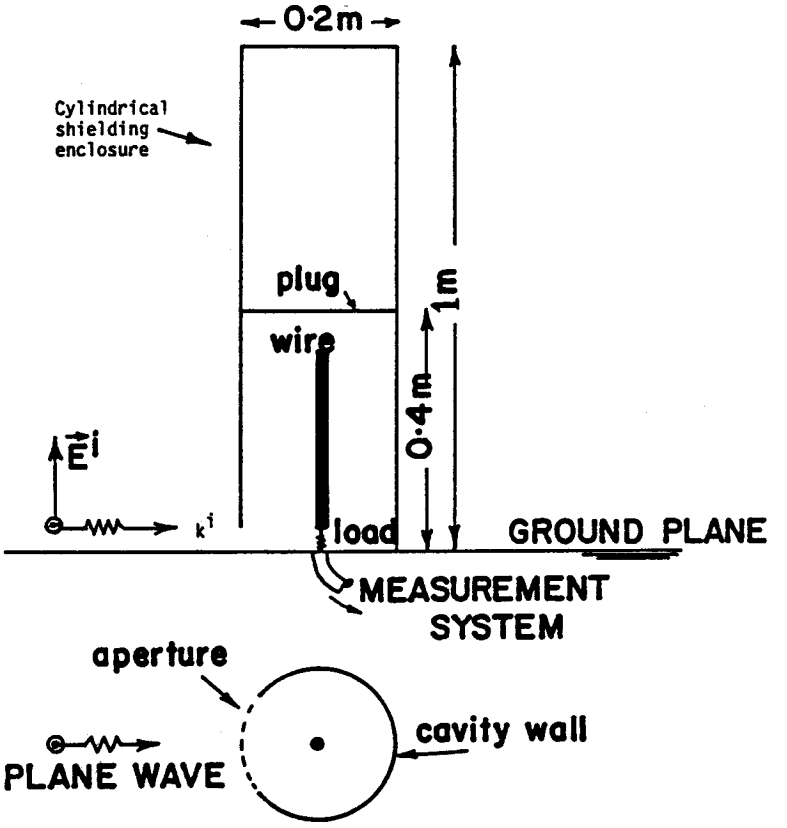

Figure 28 Geometry of the cylindrical shielding enclosure and internal wire or wire-pair [16].

Figure 27 shows an excellent correspondence between the results of the hybrid FD-TD/MOM procedure described above and the usual direct EFIE (MOM) solution for the induced current distribution on each wire of the bundle.

The hybrid FD-TD/MOM procedure for modeling thin wire bundles is most useful when the bundle is located within a shielding enclosure. Figures 28 and 29 show the geometry and test results for such a model involving the variation of induced load current with illumination frequency for a single wire and a wire-pair located at the center

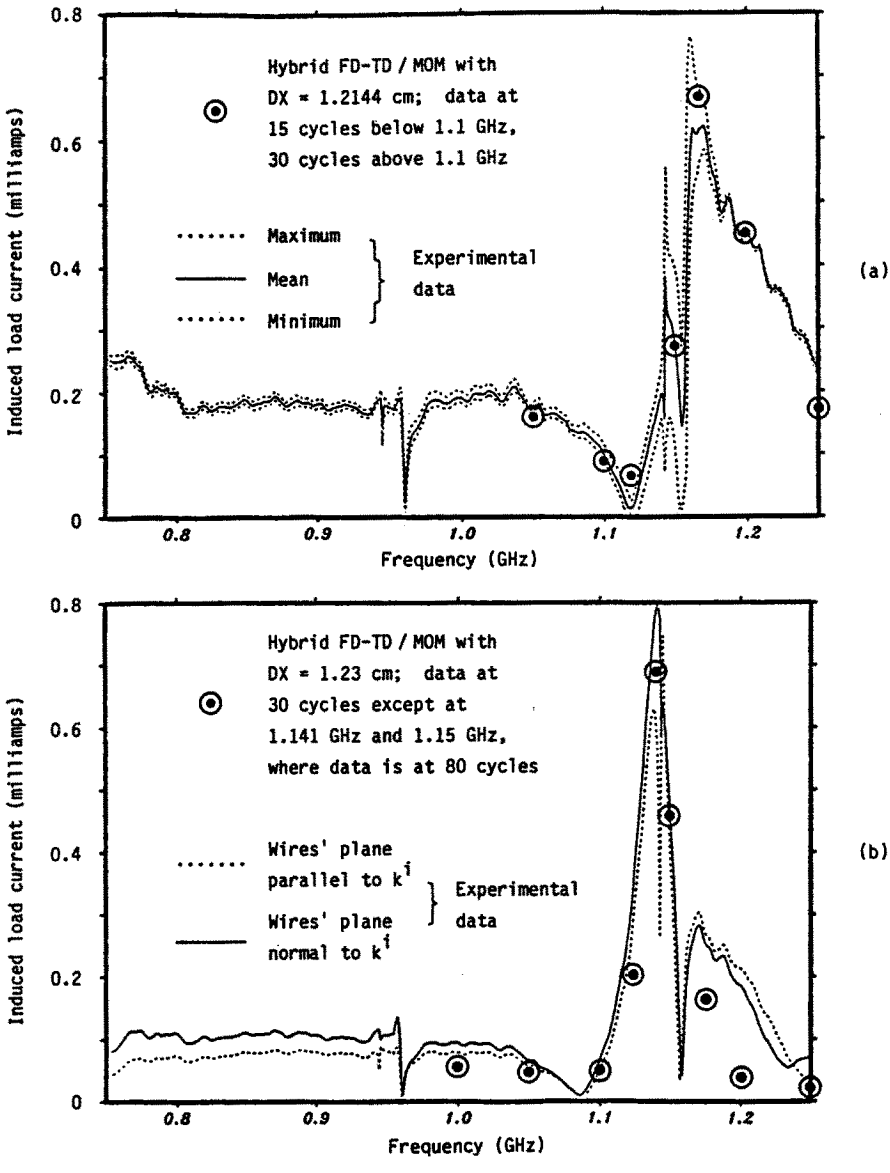

Figure 29 Comparison of hybrid FD-TD/MOM modeling predictions with experimental data for induced load current: (a) Single wire in shielding enclosure; (b) Wire-pair in shielding enclosure [16].

of a cylindrical metal enclosure [16]. The enclosure is 1.0 m high, 0.2 m in diameter, and referenced to a large metal ground plane. Approximate plane wave illumination is provided by an electrically-large conical monopole referenced to the same ground plane. Wave penetration into the interior of the enclosure is through a circumferential slot aperture (12.5 cm arc length, 1.25 cm gap) at the ground plane. For the cases studied, an internal shorting plug is located 40 cm above the ground plane. For the single-wire test, a wire of length 30 cm and radius 0.495 mm is centered within the interior and connected to the ground plane with a lumped 50-ohm load. For the wire-pair test, parallel wires of these dimensions are located 1 cm apart, with one wire shorted to the ground plane and the other connected to the ground plane with a lumped 50-ohm load. All results are normalized to a 1 volt/m incident wave electric field.

From Fig. 29, we see that there is a good correspondence between the measured and numerically modeled wire load current for both test cases. The two-wire test proved to be especially challenging since the observed Q factor of the coupling response (center frequency divided by the half-power bandwidth) is quite high, about 75. Indeed, it is found that the FD-TD code has to be stepped through as many as 80 cycles to approximately reach the sinusoidal steady state for illumination frequencies near the resonant peak [16]. However, substantially fewer cycles of time-stepping are needed away from the resonance, as indicated in the figure.

8.9 Modeling Very Complex 3-D Structures

Two characteristics of FD-TD make it very promising for numerical modeling of electromagnetic wave interactions with very complex objects. First, dielectric and permeable media can be specified independently for each electric and magnetic field vector component in the three-dimensional volume being modeled. Since there may be tens of millions of such vector components in large FD-TD models, inhomogeneous media of enormous complexity can be specified in principle. Second, the required computer resources for this type of detailed volumetric modeling are dimensionally low, only of order N, where N is the number of space cells in the FD-TD lattice.

The emergence of supercomputers has recently permitted FD-TD to be seriously applied to a number of very complex electromagnetic wave interaction problems. Two of these will now be briefly reviewed.

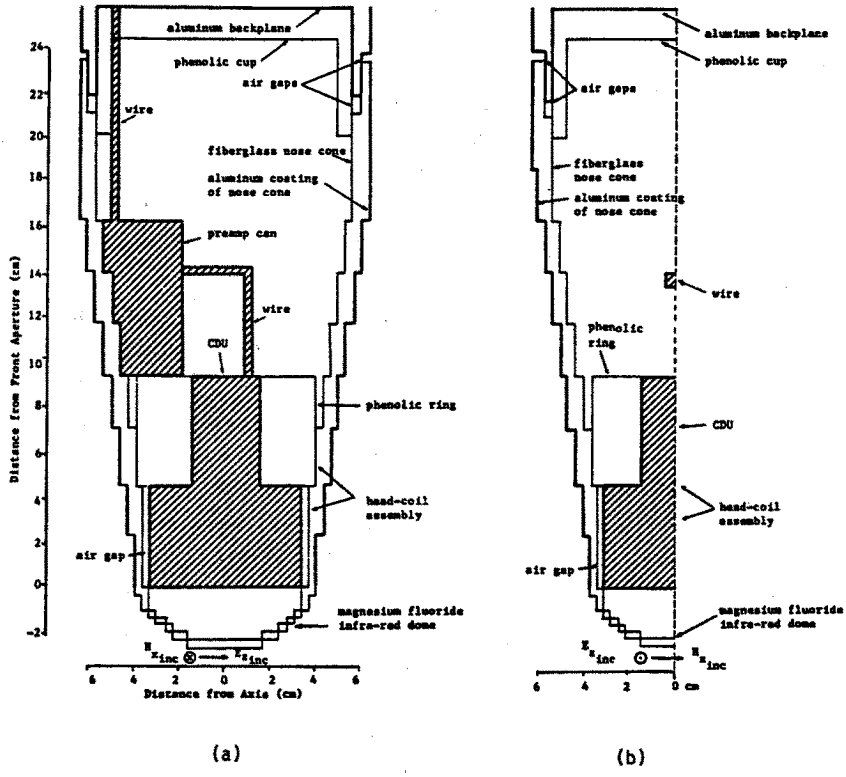

Figure 30 FD-TD model of the missile seeker section, showing component materials: (a) At the vertical symmetry plane; (b) At the horizontal observation plane [6, 37].

a. *UHF Wave Penetration into a Missile Seeker Section*

Here, FD-TD is applied to model the penetration of an axially incident 300-MHz plane wave into a metal-coated missile guidance section [6,37]. The FD-TD model, shown in Fig. 30, contains the following elements: 1. magnesium fluoride infrared dome; 2. circular nose aperture; 3. circumferential sleeve-fitting aperture 23 cm aft (loaded with Fiberglas); 4. head coil assembly; 5. cooled detector unit with enclosing phenolic ring; 6. pre-amp can; 7. wire bundle connecting the detector unit to the pre-amp can; 8. wire bundle connecting the pre-amp can to the metal backplane; and 9. longitudinal metal support rods. The Fiberglas structure of the nose cone and its metalization are

approximated in a stepped-surface manner, as is the infrared dome.

For this structure, the FD-TD model uses a uniform cell size of 1/3 cm ($\lambda_0/300$), with an overall lattice size of 24 × 100 × 48 cells containing 690,000 unknown field components. (A single symmetry plane is used, giving an effective lattice size of 48 × 100 × 48). The model is run for 1800 time steps, equivalent to 3.0 cycles of the incident wave at 300 MHz.

Figure 31 plots contour maps of the FD-TD computed field vector components at the symmetry plane of the model. An important observation is that the simulated wire bundles connecting the cooled detector unit, pre-amp can, and metal backplane are paralleled by high-level magnetic field contours (Fig. 31b). This is indicative of substantial uniform current flow along each bundle. Such current flow would generate locally a magnetic field looping around the wire bundle which, when "cut" by the symmetry plane, shows up as parallel field contours spaced equally on each side of the bundle. By using a simple Ampere's Law argument, the common-mode bundle currents can be calculated, thus obtaining a key transfer function between free-field incident UHF plane wave power density and coupled wire currents [37]. As stated earlier, this information is useful for studies of vulnerability of electronic systems to upset due to both natural and man-made electromagnetic phenomena.

Although this missile seeker model was composed to demonstrate the capability of FD-TD to map fields penetrating into a complex structure having multiple apertures and realistic internal engineering details, it should be understood that the full bistatic radar cross section pattern of the structure is available as a by-product with virtually no additional effort. Further, with the 1/3 cm space resolution used, the FD-TD radar cross section model would be useful up to 9 GHz.

b. Whole-Body Human Dosimetry at VHF and UHF Frequencies

Here, FD-TD is applied to model the penetration of plane waves at VHF and UHF frequencies into the entire human body [38,39]. Directly exploiting the ability of FD-TD to model media inhomogeneities down to the space-cell level, highly realistic three-dimensional FD-TD tissue models of the complete body have been constructed. Specific electrical parameters are assigned to each of the electric field vector components at the 16,000 to 40,000 space cells comprising the body model. Assignments are based upon detailed cross-section tissue maps

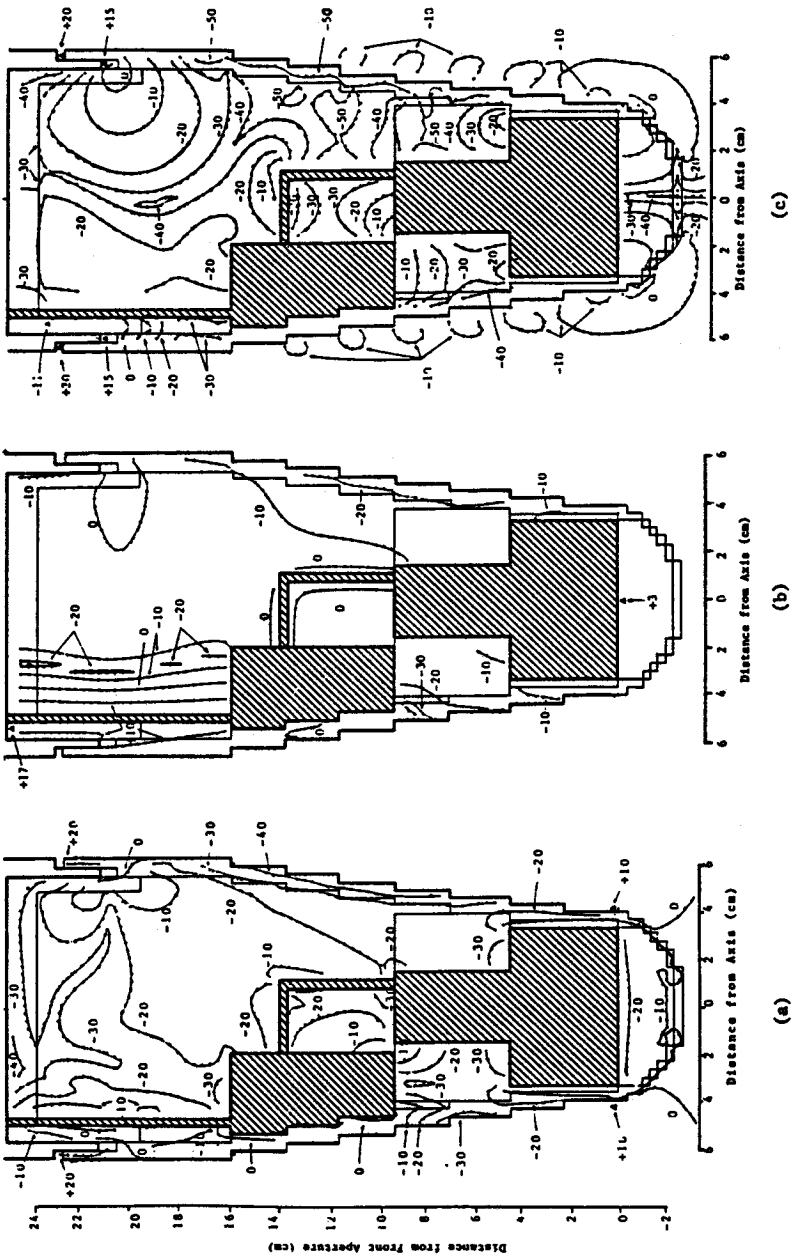

Figure 31 FD-TD computed contour maps of the penetrating fields in the vertical symmetry plane of the missile seeker section: (a) E_z; (b) H_x; (c) E_y [6,37].

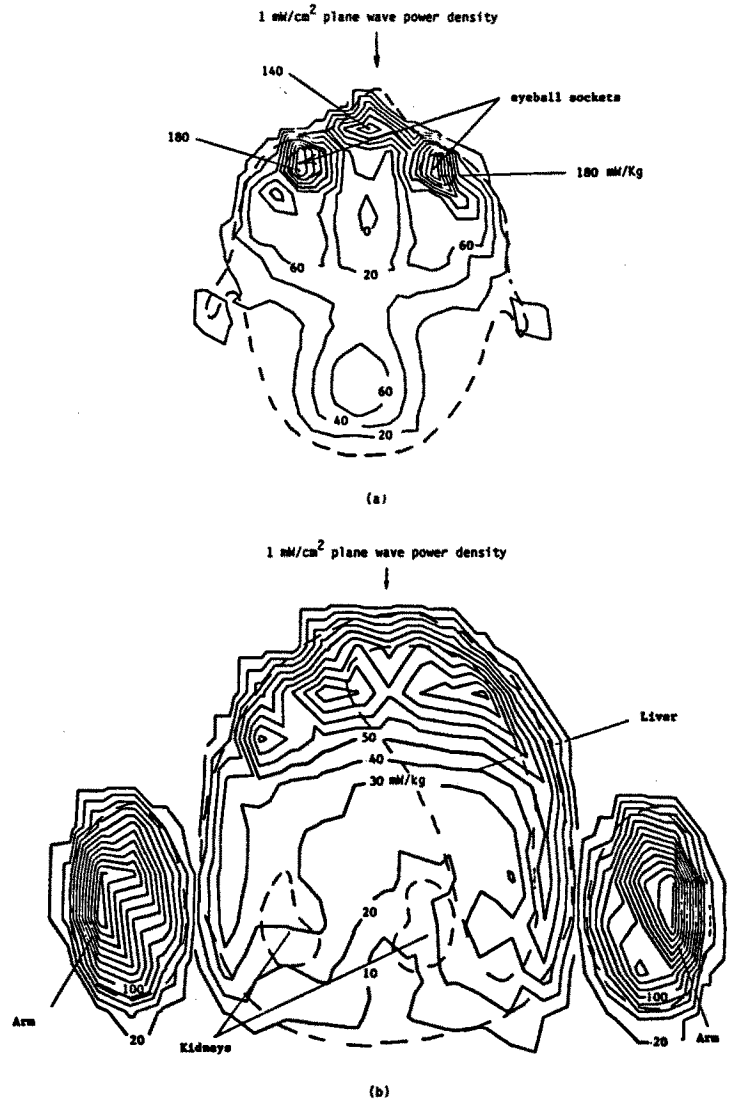

Figure 32 FD-TD computed contour maps of the specific absorption rate due to penetrating electromagnetic fields within a highly-realistic model of the entire human body: (a) Along a horizontal cut through the head at 350 MHz; (b) Along a horizontal cut through the liver at 100 MHz [39].

of the body (as obtained via cadaver studies available in the medical literature), and cataloged measurements of tissue dielectric properties. Uniform FD-TD space resolutions as fine as 1.3 cm throughout the entire human body have proven feasible with the Cray-2.

Figure 32, taken from [39], shows the FD-TD computed contour maps of the specific absorption rate (SAR) distribution along horizontal cuts through the head and liver of the three-dimensional inhomogeneous man model. In Fig. 32a, the incident wave has a power density of 1 mW/cm^2 at 350 MHz, while in Fig. 32b, the incident wave has the same power density but is at 100 MHz. These contour maps illustrate the high level of detail of local features of the SAR distribution that is possible via FD-TD modeling for highly realistic tissue models.

8.10 Microstrip and Microwave Circuits

Recently, FD-TD modeling has been extended to provide detailed characterizations of microstrips, resonators, finlines, and two-dimensional microwave circuits. In [40], FD-TD is used to calculate the dispersive characteristics of a typical microstrip on a gallium arsenide substrate. A Gaussian pulse excitation is used, and the effective dielectric constant and characteristic impedance vs. frequency is efficiently obtained over a broad frequency range via Fourier transform of the time-domain field response.

In [41], FD-TD is first used to obtain resonant frequencies of several three-dimensional cavities loaded by dielectric blocks. Next, the resonant frequency of a finline cavity is computed. Last, the resonant frequencies of a microstrip cavity on anisotropic substrate are obtained, and the dispersion characteristics of the microstrip used in the cavity are calculated. FD-TD modeling results are compared primarily to those obtained using the transmission line matrix (TLM) approach, and the two methods are found to give practically the same results.

In [42], a modified version of FD-TD is presented which provides central-difference time-stepping expressions for distributions of voltage and surface current density along arbitrary-shaped two-dimensional microwave circuits. This approach is quite different from that of [40] and [41], which utilizes the original volumetric field sampling concept for FD-TD. As a result, the method of [42] requires fewer unknowns to be solved, and avoids the need for a radiation boundary condition. However, an auxiliary condition is required to describe the loading effects of the fringing fields at the edges of the microstrip conducting

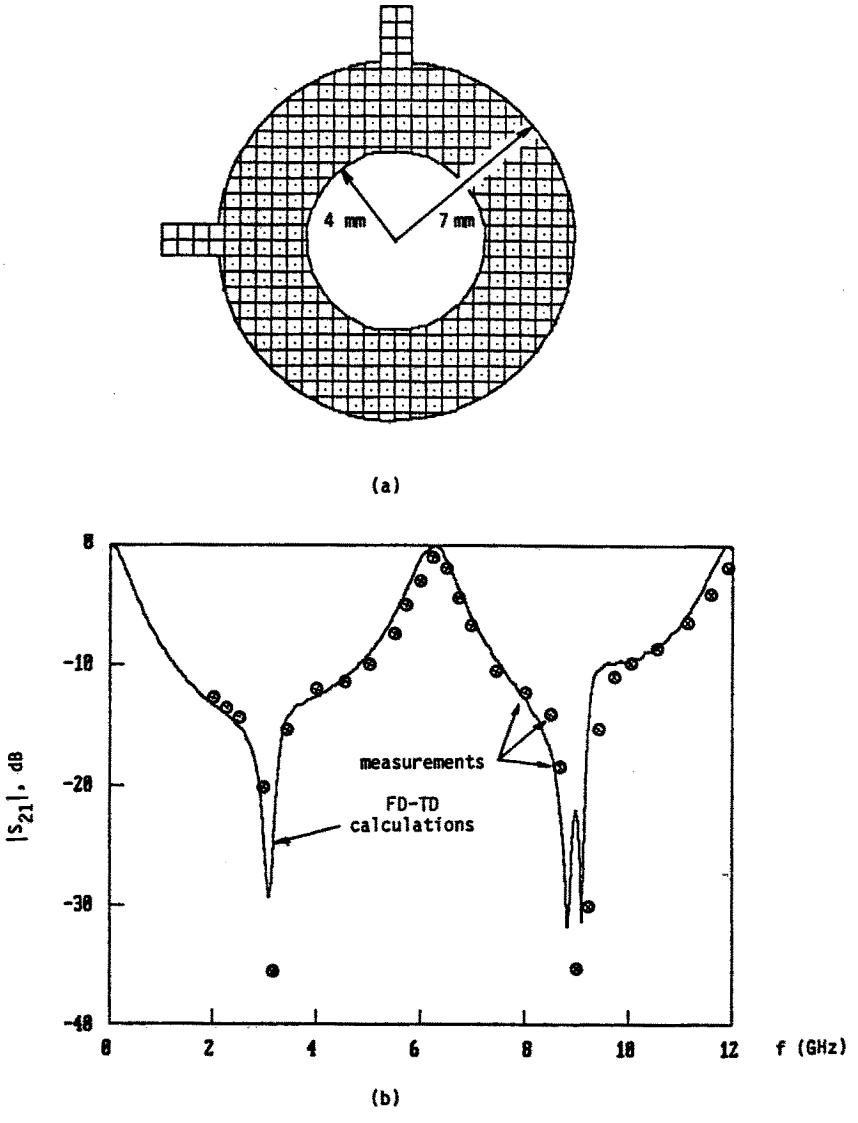

Figure 33 Comparison of FD-TD modeling predictions with measurements of $|S_{21}|$ for a two-port microstrip ring circuit: (a) Geometry and gridding of microstrip circuit; (b) Comparative results over 2–12 GHz [42].

paths. Figure 33, taken from [42], shows the FD-TD computed S parameter, $|S_{21}|$, as a function of frequency for a two-port microstrip ring circuit. The ring circuit, gridded as shown in the figure, has an inner radius of 4 mm, outer radius of 7 mm, substrate relative permittivity of 10 and relative permeability of 0.93 (simulating duroid), and is connected to two 50-ohm lines making a 90° angle. The broadband response of the circuit is obtained using a single FD-TD run for an appropriate pulse excitation, followed by Fourier transformation of the desired response time-domain waveform. From Fig. 33, we see good agreement of the predicted and measured circuit response over the 2–12 GHz frequency band and a dynamic range of about 30 dB. [42] concludes that the application of its FD-TD approach to arbitrarily-shaped microstrip circuits is encouraging, but more work is needed to determine the modeling limitations, especially at higher frequencies where media dispersion can become important.

8.11 Inverse Scattering Reconstructions

Initial work has demonstrated the possibility of accurately reconstructing one-dimensional profiles of permittivity and conductivity [43], and the shape and dielectric compositions of two-dimensional targets [44,45] from minimal scattered field pulse response data. The general approach involves setting up a numerical feedback loop which uses a one- or two-dimensional FD-TD code as a forward-scattering element, and a specially constructed non-linear optimization code as the feedback element. FD-TD generates a test pulse response for a trial layering or target shape/composition. The test pulse is compared to the measured pulse, and an error signal is developed. Working on this error signal, the non-linear optimization element perturbs the trial layering or target shape/composition in a manner to drive down the error. Upon repeated iterations, the proposed layering or target ideally converges to the actual one, a strategy similar to that of [46].

The advantage of working in the time domain is that a layered medium or target shape can be reconstructed sequentially in time as the wavefront of the incident pulse sweeps through, taking advantage of causality. This reduces the complexity of reconstruction since only a portion of the layering or target shape is being generated at each iteration. Advanced strategies for reconstruction in the presence of additive noise may involve the use of prediction/correction, where the trial layer or target shape is considered to be a predictor of the actual

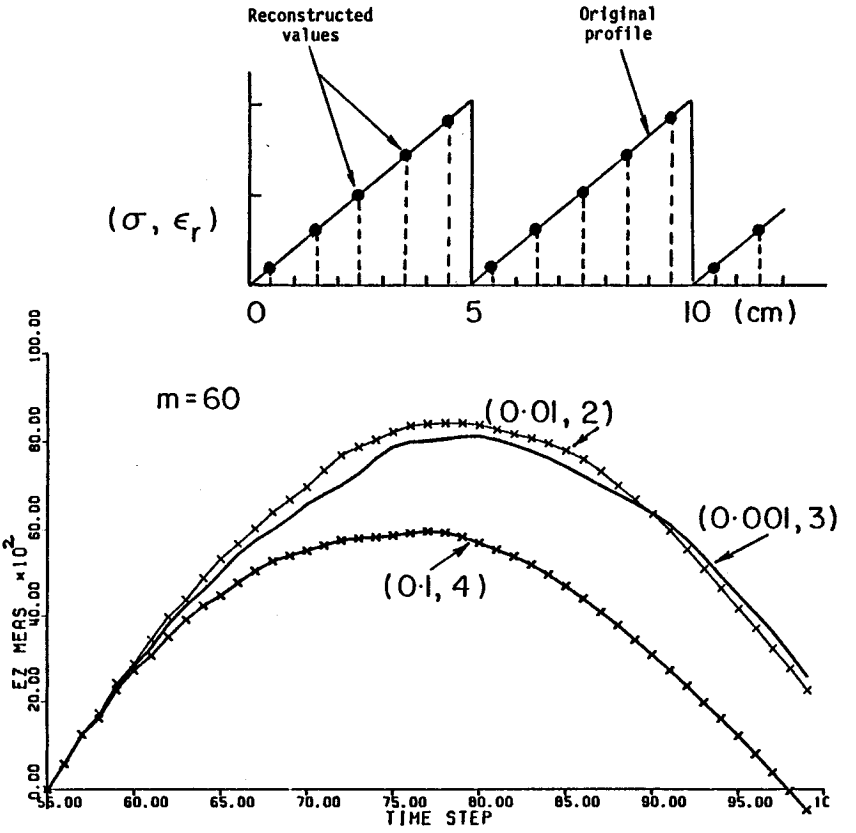

Figure 34 Application of the FD-TD/feedback strategy to reconstruct a 1-D sawtooth variation of electrical permittivity and conductivity in the absence of noise [43].

case, which is subsequently corrected by optimization of the entire layered medium or target shape using the complete scattered pulse waveform.

Figure 34 shows the application of the basic FD-TD feedback strategy to a one-dimensional layered medium in the absence of noise. Both the electrical permittivity and conductivity of the medium vary in a "sawtooth" manner with depth. The curves show simulated measured data for the reflected pulse for three cases defined by the peak values of the conductivity (0.001 S/m, 0.01 S/m, and 0.1 S/m) and the corresponding spatially coincident peak values of relative permittivity (3, 2, and 4) of the medium. In each case, the incident pulse is

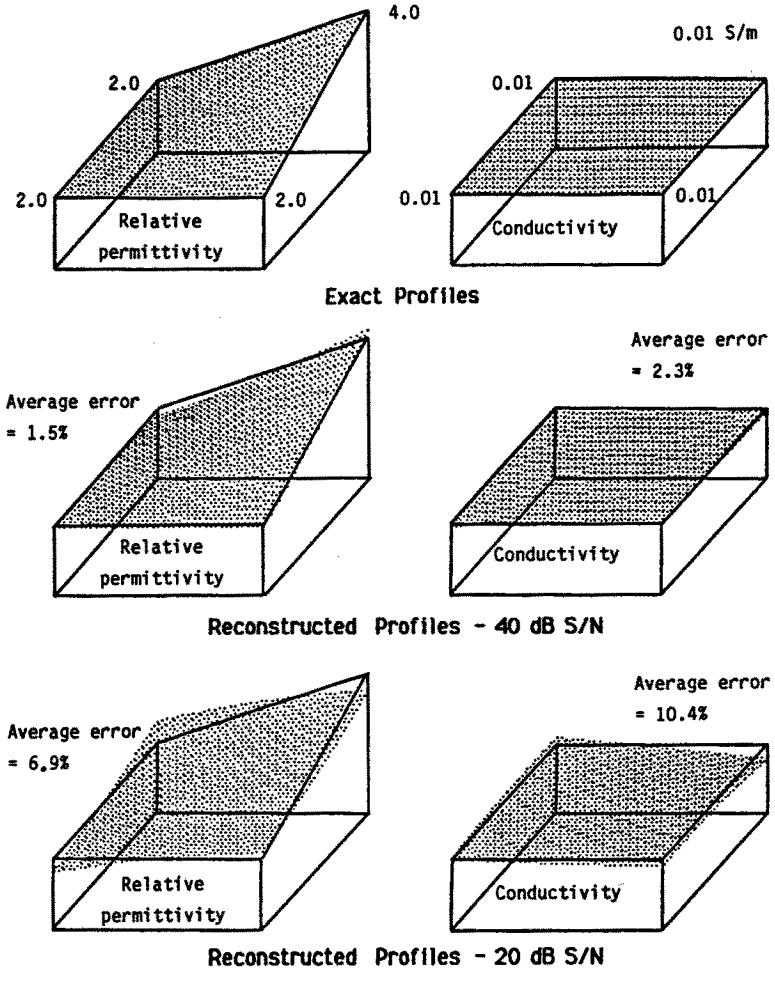

Figure 35 Application of the FD-TD/feedback strategy to reconstruct a 2-D lossy dielectric target in the presence of noise [45].

assumed to be a half-sinusoid spanning 50 cm between zero crossings. Noting that the dark dots superimposed on the "sawtooth" represent the reconstructed values of permittivity and conductivity, we see that the basic FD-TD feedback strategy is quite successful in the absence of noise [43].

Figure 35 shows the application of the FD-TD feedback strategy to reconstruct a two-dimensional lossy dielectric target. The target is a 30 cm $\times$ 30 cm square cylinder having a uniform conductivity of 0.01

S/m, and a tent-like relative permittivity profile which starts at 2.0 at the front and left sides and increases linearly to a peak value of 4.0 at the back corner on the right side. These profiles are illustrated in a perspective manner at the top of Fig. 35. The target is assumed to be illuminated by a TM polarized plane wave that is directed toward the front of the target (as visualized at the top of the figure). The incident waveform is a 3-cycle sinusoidal tone burst having a 60-MHz carrier frequency. For the reconstruction, the only data set utilized is the time-domain waveform of the scattered electric field, as observed at two points. These points are located 1 m from the front of the target, and are positioned 15 cm to either side of the target center line. To simulate measured data, the FD-TD computed scattered field waveforms are contaminated with additive Gaussian noise. In all of the reconstructions, the target shape and location are assumed to be known.

From Fig. 35, we see that for a signal/noise ratio of 40 dB, the average error in the reconstructed permittivity and conductivity profiles is 1.5% and 2.3%, respectively. If the signal/noise ratio is reduced to 20 dB, the average errors increase to 6.9% and 10.4%, respectively [45]. Research is ongoing to determine means of improving the noise performance, especially using predictor/corrector techniques briefly discussed earlier. Given the relatively small amount of scattered field data utilized, the FD-TD feedback strategy appears promising for future development.

8.12 Very Large-Scale Software

The FD-TD method is naturally suited for large-scale processing by state-of-the-art vector supercomputers and concurrent processors. This is because essentially all of the arithmetic operations involved in a typical FD-TD run can be vectorized or cast into a highly concurrent format. Further, the $O(N)$ demand for computer memory and clock cycles (where N is the number of lattice space cells) is dimensionally low. This permits three-dimensional FD-TD models of structures spanning 50–100 λ_0 to be anticipated in the early 1990's.

Let us now consider computation times of present FD-TD codes. Table 1 lists computation times (derived either from benchmark runs or based on analysts' estimates) for modeling one illumination angle of a 10-λ_0 three-dimensional structure using the present FD-TD code. Note that the fourth computing system listed in the table is a hypothetical

next-generation machine operating at an average rate of 10 Gflops. This capability is generally expected to be available in the early 1990's.

Table 1. Computation Times

Machine	Time †
VAX 11/780 (no floating point accelerator)	40 hours
Cray-2 (single processor, using VAX Fortran)	12 min
Cray-2 (single processor, with optimization)	2 min
Cray-2 (four processors, with optimization)	30 sec (est.)
True 10 Gflop machine	2 sec (est.)

From Table 1, it is fairly clear that steadily advancing supercomputer technology will permit routine engineering usage of FD-TD for modeling electromagnetic wave interactions with electrically-large structures by 1995.

An interesting prospect that has recently arisen is the reduction of the $O(N)$ computational burden of FD-TD to $O(N^{1/3})$. This possibility is a consequence of the appearance of the Connection Machine (CM), which has tens of thousands of simple processors and associated memories arranged in a highly efficient manner for processor-to-processor communication. With the CM, a single processor could be assigned to store and time-step a single row of vector field components in a three-dimensional FD-TD space lattice. For example, $1.5 \cdot 10^6$ processors would be sufficient to store the 6 Cartesian components of E and H for each of the 500×500 rows of a cubic lattice spanning $50\lambda_0$ (assuming 10 cells/λ_0 resolution). FD-TD time-stepping would be performed via row operations mapped onto the individual CM processors. These row operations would be performed concurrently. Thus, for a fixed number of time steps, the total running time would be proportional to the time needed to perform a single row operation, which

† Computation times are for the 9-wavelength T-shaped target using the present FD-TD code. There are 1.55×10^6 unknown field vector components and 661 time steps. The complete bistatic RCS pattern is obtained for a single illumination angle at a single frequency. Times are increased by 50%-100% if an impulsive illumination / Fourier transform is used to obtain the bistatic RCS pattern at a multiplicity of frequencies within the spectrum of the impulsive illumination.

in turn would be proportional to the number of field vector components in the row, or $O(N^{1/3})$.

For the 50-λ_0 cubic lattice noted above, this would imply a dimensional reduction of the computational burden from $O(500^3)$ to $O(500)$, a tremendous benefit. As a result, it is conceivable that a suitably scaled CM could model one illumination angle of a 50-λ_0 three-dimensional structure in only a few seconds, achieving effective floating-point rates in the order of 100 Gflops. For this reason, FD-TD software development for the CM is a promising area of research for developing ultra-large numerical models of electromagnetic wave interactions with complex structures.

8.13 Conclusion

This chapter has reviewed the basic formulation of the FD-TD numerical modeling approach for Maxwell's equations. A number of two- and three-dimensional examples of FD-TD modeling of electromagnetic wave interactions with structures were provided to indicate the accuracy and breadth of FD-TD applications. The objects modeled range in nature from simple geometric shapes to extremely complex aerospace and biological systems. In all cases studied to date where rigorous analytical, code-to-code, or experimental validations were possible, FD-TD predictive data for penetrating and scattered near fields as well as radar cross section were in excellent agreement with benchmark data. It was also shown that opportunities are arising in applying FD-TD to model rapidly time-varying systems, microwave circuits, and inverse scattering. With continuing advances in FD-TD modeling theory, as well as continuing advances in vector and concurrent supercomputer technology, there is a strong possibility that FD-TD numerical modeling will occupy an important place in high-frequency engineering electromagnetics as we move into the 1990's.

Acknowledgements

The authors wish to acknowledge the research contributions of their colleague, Prof. Gregory A. Kriegsmann of Northwestern University, Department of Engineering Science and Applied Mathematics. Contributions of graduate students at Northwestern and the University of Illinois at Chicago, especially Mr. Ben Beker, Mr. Jeffrey Blaschak,

Mr. Fady Harfoush, Mr. Thomas Jurgens, Mr. Thomas Moore, and Mr. Mark Strickel are also gratefully acknowledged.

The authors also wish to acknowledge the support of their sponsors, past and present, including the U.S. Air Force Rome Air Development Center (Contracts F30602-77-C-0163, F30602-79-C-0039, F30602-80-C-0302, and F19628-82-C-0140); Lawrence Livermore National Laboratory (Contract 6599805); NASA Lewis Research Center (Grant NAG 3-635); National Science Foundation (Grants ECS-8515777 and ASC-8811273); Office of Naval Research (Contract N00014-88-K-0475); General Dynamics (PO-4059045); and Cray Research Inc.

References

[1] Yee, K. S., "Numerical solution of initial boundary value problems involving Maxwell's equations in isotropic media," *IEEE Trans. Antennas Propagat.*, **AP-14**, 302–307, 1966.

[2] Taflove, A., and M. E. Brodwin. "Numerical solution of steady-state electromagnetic scattering problems using the time-dependent Maxwell's equations," *IEEE Trans. Microwave Theory Tech.*, **MTT-23**, 623–630, 1975.

[3] Kriegsmann, G. A., "Exploiting the limiting amplitude principle to numerically solve scattering problems," *Wave Motion*, **4**, 371–380, 1982.

[4] Taflove, A., and M. E. Brodwin. "Computation of the electromagnetic fields and induced temperatures within a model of the microwave-irradiated human eye," *IEEE Trans. Microwave Theory Tech.*, **MTT-23**, 888–896, 1975.

[5] Taflove, A., "Application of the finite-difference time-domain method to sinusoidal steady state electromagnetic penetration problems," *IEEE Trans. Electromagn. Compat.*, **EMC-22**, 191–202, 1980.

[6] Taflove, A., and K. R. Umashankar, "A hybrid moment method/finite-difference time-domain approach to electromagnetic coupling and aperture penetration into complex geometries," *IEEE Trans. Antennas Propagat.*, **AP-30**, 617–627, 1982.

[7] Holland, R., "Threde: A free-field EMP coupling and scattering code," *IEEE Trans. Nuclear Sci.*, **NS-24**, 2416–2421, 1977.

[8] Kunz, K. S., and K. M. Lee, "A three-dimensional finite-difference solution of the external response of an aircraft to a complex transient EM environment: Part I, The method and its implementation," *IEEE Trans. Electromagn. Compat.*, **EMC-20**, 328–333, 1978.

[9] Merewether, D. E., R. Fisher, and F. W. Smith, "On implementing a numeric Huygens' source scheme in a finite-difference program to illuminate scattering bodies," *IEEE Trans. Nuclear Sci.*, **NS-27**, 1819–1833, 1980.

[10] Taflove, A., and K. R. Umashankar, "Advanced numerical modeling of microwave penetration and coupling for complex structures," Final Rept. No. UCRL-15960, Contract 6599805, Lawrence Livermore Nat. Lab., 1987.

[11] Mur, G., "Absorbing boundary conditions for the finite- difference approximation of the time-domain electromagnetic field equations," *IEEE Trans. Electromagn. Compat.*, **EMC-23**, 377–382, 1981.

[12] Umashankar, K. R., and A. Taflove, "A novel method to analyze electromagnetic scattering of complex objects," *IEEE Trans. Electromagn. Compat.*, **EMC-24**, 397–405, 1982.

[13] Taflove, A., and K. R. Umashankar, "Radar cross section of general three-dimensional scatterers," *IEEE Trans. Electromagn. Compat.*, **EMC-25**, 433–440, 1983.

[14] Taflove, A., K. R. Umashankar, and T. G. Jurgens, "Validation of FD-TD modeling of the radar cross section of three-dimensional structures spanning up to nine wavelengths," *IEEE Trans. Antennas Propagat.*, **AP-33**, 662–666, 1985.

[15] Taflove, A., K. R. Umashankar, B. Beker, F. Harfoush, and K. S. Yee, "Detailed FD-TD analysis of electromagnetic fields penetrating narrow slots and lapped joints in thick conducting screens," *IEEE Trans. Antennas Propagat.*, **AP-36**, 247–257, 1988.

[16] Umashankar, K. R., A. Taflove, and B. Beker, "Calculation and experimental validation of induced currents on coupled wires in an arbitrary shaped cavity," *IEEE Trans. Antennas Propagat.*, **AP-35**, 1248–1257, 1987.

[17] Engquist, B., and A. Majda, "Absorbing boundary conditions for the numerical simulation of waves," *Math. Comp.*, **31**, 629–651, 1977.

[18] Trefethen, L. N., and L. Halpern, "Well-posedness of one-way wave equations and absorbing boundary conditions," *Inst. Comput. Appl. Sci. and Engrg.* (ICASE), NASA Langley Res. Ctr., Hampton, VA, Rept. 85-30, 1985.

[19] Moore, T. G., J. G. Blaschak, A. Taflove, and G. A. Kriegsmann, "Theory and application of radiation boundary operators," *IEEE Trans. Antennas Propagat.*, **AP-36**, 1988 (in press).

[20] Blaschak, J. G., and G. A. Kriegsmann, "A comparative study of absorbing boundary conditions," *J. Computational Physics*, **77**, 109–139, 1988.

[21] Borup, D. T., D. M. Sullivan, and O. P. Gandhi, "Comparison of the FFT conjugate gradient method and the finite-difference time-domain method for the 2-D absorption problem," *IEEE Trans. Microwave Theory Tech.*, **MTT-35**, 383–395, 1987.

[22] Beker, B., K. R. Umashankar, and A. Taflove, "Numerical analysis and validation of the combined-field surface integral equations for electromagnetic scattering by arbitrary shaped two-dimensional anisotropic objects," *IEEE Trans. Antennas Propagat.*, **AP-37**, 1989.

[23] Taflove, A., and K. R. Umashankar, "Analytical models for electromagnetic scattering," Final Rept. RADC-TR-85-87, Contract F19628-82-C-0140, Electromagn. Sci. Div., Rome Air Dev. Center., Hanscom AFB, Mass., 1985.

[24] Jurgens, T. G., A. Taflove, and K. R. Umashankar, "FD-TD conformal modeling of smooth curved surfaces," presented at URSI Radio Science Meeting, Blacksburg, Virginia, June, 1987.

[25] Madsen, N. K., and R. W. Ziolkowski, "Numerical solution of Maxwell's equations in the time domain using irregular nonorthogonal grids," *Wave Motion*, **10**, 1988 (in press).

[26] Fusco, M., "FD-TD algorithm in curvilinear coordinates," *IEEE Trans. Antennas Propagat.*, submitted.

[27] McCartin, B., L. J. Bahrmasel, and G. Meltz, "Application of the control region approximation to two-dimensional electromagnetic scattering," Chap. 5 in this text.

[28] Shankar, V., and W. Hall, "A time-domain differential solver for electromagnetic scattering problems," *Proc. IEEE*, **77**, 1989 (in press).

[29] Blaschak, J. G., G. A. Kriegsmann, and A. Taflove, "A study of wave interactions with flanged waveguides and cavities using the

on-surface radiation condition method," *Wave Motion*, **19**, 1989 (in press).

[30] Harfoush, F., A. Taflòve, and G. A. Kriegsmann, "A numerical technique for analyzing electromagnetic wave scattering from moving surfaces in one and two dimensions," *IEEE Trans. Antennas Propagat.*, **AP-37**, 1989 (in press).

[31] Harfoush, F., A. Taflove, and G. A. Kriegsmann, "Numerical implementation of relativistic electromagnetic field boundary conditions in a laboratory-frame grid," *J. Computational Physics*, accepted for publication.

[32] De Zutter, D., "Reflections from linearly vibrating objects: plane mirror at oblique incidence," *IEEE Trans. Antennas Propagat.*, **AP-30**, 898–903, 1982.

[33] Wilton, D. R., and S. Govind, "Incorporation of edge conditions in moment method solutions," *IEEE Trans. Antennas Propagat.*, **AP-25**, 845–850, 1977.

[34] Gilbert, J., and R. Holland, "Implementation of the thin-slot formalism in the finite-difference EMP code THREDII," *IEEE Trans. Nuclear Sci.*, **NS-28**, 4269–4274, 1981.

[35] Yee, K. S., "A numerical method of solving Maxwell's equations with a coarse grid bordering a fine grid," SGEMP Note #9, Document D-DV-86-0008, D Division, Lawrence Livermore Nat. Lab., 1986.

[36] Holland, R., and L. Simpson, "Finite-difference analysis of EMP coupling to thin struts and wires," *IEEE Trans. Electromagn. Compat.*, **EMC-23**, 88–97, 1981.

[37] Taflove, A., and K. R. Umashankar, "Evaluation of time-domain electromagnetic coupling techniques. Vol. I: Theory and numerical results," Final Rept. RADC-TR-80-251, Contract F30602-79-C-0039, Rome Air Dev. Center, Griffiss AFB, NY, 1980.

[38] Sullivan, D. M., D. T. Borup, and O. P. Gandhi, "Use of the finite-difference time-domain method in calculating EM absorption in human tissues," *IEEE Trans. Biomed. Engr.*, **BME-34**, 148–157, 1987.

[39] Sullivan, D. M., O. P. Gandhi, and A. Taflove, "Use of the finite-difference time-domain method for calculating EM absorption in man models," *IEEE Trans. Biomed. Eng.*, **35**, 179–186, 1988.

[40] Zhang, X., J. Fang, K. K. Mei, and Y. Liu, "Calculations of the dispersive characteristics of microstrips by the time-domain finite-

difference method," *IEEE Trans. Microwave Theory Tech.*, **MTT-36**, 263–267, 1988.

[41] Choi, D. H., and W. J. Hoefer, "The finite-difference time-domain method and its application to eigenvalue problems," *IEEE Trans. Microwave Theory Tech.*, **MTT-34**, 1464–1470, 1986.

[42] Gwarek, W. K., "Analysis of arbitrarily-shaped two-dimensional microwave circuits by the finite-difference time-domain method," *IEEE Trans. Microwave Theory Tech.*, **MTT-36**, 738–744, 1988.

[43] Umashankar, K. R., S. K., Chaudhuri, and A. Taflove, "Finite-difference time-domain formulation of an inverse scattering scheme for remote sensing of inhomogeneous lossy layered media," *IEEE Trans. Antennas Propagat.*, submitted.

[44] Strickel, M. A., A. Taflove, and K. R. Umashankar, "Accurate reconstruction of two-dimensional conducting and homogeneous dielectric target shapes from a single-point TM scattered field pulse response," *IEEE Trans. Antennas Propagat.*, submitted.

[45] Strickel, M. A., and A. Taflove, "Reconstruction of one- and two-dimensional inhomogeneous dielectric targets using the FD-TD/feedback method," *IEEE Trans. Antennas Propagat.*, submitted.

[46] Bennett, C. L., and G. F. Ross, "Time-domain electromagnetics and its applications," *Proc. IEEE*, **66**, 299–318, 1978.